Additive Manufacturing 121 (2026) 105165

Contents lists available at ScienceDirect

Additive Manufacturing

journal homepage: www.elsevier.com/locate/addma

Crystallization during laser powder bed fusion of the Finemet soft magnetic glass-forming alloy

S. Sadanand [a,b], A.D. Boccardo [c], B. Yang [a], M. Rodríguez-Sánchez [a,b], A. Ghavimi [d], R. Busch [d], I. Gallino [e], M.T. Pérez-Prado [a,*]

[a] IMDEA Materials Institute, Calle Eric Kandel, 2, Getafe, Madrid 28906, Spain
[b] Materials Science and Engineering Dept., Carlos III University, Av. de la Universidad, 30, Leganés, Madrid 28911, Spain
[c] Durability and Mechanical Integrity of Structural Materials group (DIMME), Universidad Rey Juan Carlos, C/Tulipán, s/n. 28933 Móstoles, Madrid, Spain
[d] Saarland University, Chair of Metallic Materials, Campus C6.3, Saarbrücken 66123, Germany
[e] Technical University of Berlin, Chair of Metallic Materials, Ernst-Reuter Platz 1, Berlin 10587, Germany

ARTICLE INFO

Keywords:
Laser powder bed fusion
Finemet
Fe-based metallic glasses
Crystallization
Nucleation and growth
Numerical simulation

ABSTRACT

This study investigates crystallization phenomena during laser powder bed fusion (LPBF) of the soft magnetic, glass-forming Finemet® alloy. Cuboidal specimens were fabricated using a double-scan strategy, in which the scan speed of the second pass was varied to tailor local thermal conditions. The resulting microstructures were characterized using optical, scanning, and transmission electron microscopy, while thermal histories were modeled through finite element (FEM) simulations. The results are interpreted within the framework of classical nucleation and growth theory. The LPBF-processed material exhibits a mixed amorphous–crystalline microstructure, with equiaxed crystallites predominantly formed by partial devitrification of previously deposited amorphous regions. These equiaxed grains resemble those produced during the devitrification of melt-spun ribbons, being enriched in Fe and Si, depleted in Nb and B, and displaying a DO_3 structure. However, their size distribution is substantially broader, ranging from a few tens to several hundred nanometers. This gradient, coarse microstructure is attributed to the extreme thermal conditions inherent to LPBF, which vary locally within the heat-affected zone, and to the reduced Cu cluster density resulting from rapid solidification. Additionally, a minor population of dendritic crystals develops at the melt pool peripheries during solidification, with their size decreasing as scan speed increases, consistent with higher FEM-simulated cooling rates. Precise tailoring of the amorphous–crystalline microstructure is key to the integration of the investigated material into complex-shaped components for energy applications.

1. Introduction

Metallic glasses (MGs), or amorphous metals, represent a unique class of materials that deviate from conventional crystalline metals by exhibiting a disordered atomic structure [1–7]. First discovered in the 1960s [8], MGs have since evolved into a broad family of materials, including binary and multicomponent systems, covering a range of elemental compositions. Their distinctive structure, in the absence of grain boundaries and other crystalline defects commonly found in traditional metals, imparts exceptional mechanical [9,10], magnetic [11], and corrosion-resistant [12] properties, making them attractive for applications across electronics, biomedical devices, structural components, and energy systems [13,14].

Despite their outstanding properties, metallic glasses face significant limitations in manufacturability, particularly in forming bulk, complex-shaped components [15]. This stems from their high critical cooling rates (often exceeding 10^5–10^6 °C/s), which restrict the production of fully amorphous structures to thin ribbons, foils, or powders in many systems. While advancements in alloy design have led to the development of bulk metallic glasses (BMGs) with lower critical cooling rates [6,7], these remain constrained in size and geometry when processed using traditional casting techniques. Furthermore, metallic glasses are unstable by nature, and their thermodynamic tendency to undergo physical aging and eventually crystallize upon thermal exposure [16–20] presents a challenge not only during processing but also in service operation where thermal excursions may occur. Crystallization in metallic glasses

* Corresponding author.
E-mail address: teresa.perez.prado@imdea.org (M.T. Pérez-Prado).

https://doi.org/10.1016/j.addma.2026.105165
Received 23 October 2025; Received in revised form 2 March 2026; Accepted 12 March 2026
Available online 15 March 2026

Table 1
LPBF printing parameters.

Sample	Melting cycle	P (W)	v (mm/s)	t_{exp} (μs)	VED (J/mm^3)
S1	1st scan	60	500	150	50
	2nd scan	60	500	150	50
S2	1st scan	60	500	150	50
	2nd scan	60	890	80	30

is a complex process that depends on alloy chemistry [21], thermal history [22], and external stimuli such as stress [23] or irradiation [24]. Typically, it proceeds through nucleation and growth mechanisms, governed by the competition between thermodynamic driving forces and kinetic barriers [4]. Primary crystallization involves the formation of a single crystalline phase via a solid-solid state transformation that involves the nucleation and growth of crystals within the amorphous matrix, while secondary solid-solid crystallizations may follow of the type amorphous-to-crystalline or crystalline-to-crystalline forming a mixture of multiple crystalline phases or intermetallic compounds. Understanding the crystallization mechanisms is crucial to the stability and performance of MGs, and thus to expand their practical applications and integrate them into complex, high-performance systems.

Among metallic glass systems, many Fe-based alloys stand out for their excellent soft magnetic properties, high saturation magnetization, low coercivity, high electrical resistivity, and relatively low cost [25]. These characteristics make them ideal candidates for use in electrical transformers, inductors, magnetic sensors, and motor cores [26,27]. One notable example of a commercially in use alloy is the Finemet® alloy, with typical composition $Fe_{73.5}Si_{13.5}B_9Nb_3Cu_1$ at%. This glass-forming alloy was however designed in a way that fully amorphous as-spun ribbons could judiciously be partially devitrified after the winding into a composite formed by Fe_3Si nanocrystallites (~10–20 nm in size) embedded within the amorphous matrix to enhance the soft magnetic properties for the passive motor components [28,29]. The crystallization behavior of Finemet in the form of as-spun ribbons has been widely studied under isothermal and continuous heating conditions, where it exhibits a characteristic two-stage crystallization: initial formation of Fe-Si nanocrystals, triggered by the presence of Cu clusters, followed by the growth of Fe–B and Fe–Nb-based intermetallics [30,31]. Niobium, owing to its large atomic size and sluggish diffusion, partitions into the amorphous matrix where it impedes the crystal growth [28]. Boron also partitions to the matrix and has a critical role in stabilizing the amorphous phase [28]. The ability to finely tune nanocrystalline microstructures through precise thermal treatments has enabled the optimization of Finemet's magnetic response.

Laser powder bed fusion (LPBF) offers the possibility of fabricating complex, near-net-shape components with high spatial resolution [32]. The rapid solidification conditions inherent to LPBF, involving cooling rates that include the 10^5-10^6 °C/s range, steep thermal gradients, and localized melting, mirror those required for metallic glass formation, positioning LPBF as a promising route for the additive manufacturing of metallic glass components [33–36]. Furthermore, LPBF enables local tailoring of thermal cycles, offering potential pathways for in situ control of the (micro)structure, including the fraction of amorphous and nanocrystalline regions [37–40]. While successful fabrication of amorphous structures using LPBF has been demonstrated in selected systems [41–51], maintaining a fully glassy phase remains challenging in alloys with medium to low glass forming ability (GFA) and with critical casting thicknesses below 1 mm due to the intrinsic thermal cycling of the layer-by-layer process and heat accumulation from successive layers. This problem is exacerbated in alloys with critical casting thicknesses of 100–200 μm, such as Finemet [52,53] and other commercial Fe-based metallic glasses [54,55], which have thus been so far manufactured mostly by melt spinning [56,57], as high energy conditions that eliminate lack of fusion defects lead to unwanted devitrification. Crystallization during LPBF might take place either during rapid solidification of the molten pool, if the local cooling rate falls below the minimum value required to stabilize the amorphous phase in a particular composition, or in the heat-affected zone (HAZ) during subsequent laser passes [58]. Only two recent studies [52,53], including our own work [52] explored additive manufacturing routes via laser powder bed fusion (LPBF) to process the Finemet composition. A thorough understanding of the crystallization behavior in Finemet during LPBF, which is currently missing, would be essential to unlock the full potential of AM to manufacture bulk, complex-shaped components using this material.

The aim of this work is to investigate the crystallization phenomena during LPBF of the soft magnetic Finemet alloy and to relate the nature of the resulting crystallites to the processing parameters. To this end, microstructural characterization has been conducted at multiple length scales, together with finite element (FEM) simulations, to reveal how LPBF parameters influence the size, morphology, phase structure, and local chemical composition of the crystallites formed during processing. These features will be compared to those observed in crystallites formed through conventional processing routes for this alloy, such as isothermal annealing and flash annealing of melt-spun ribbons. The results are discussed in terms of the classical crystal nucleation and growth theory.

2. Experimental procedure

2.1. Material

Commercially available Finemet alloy powders were sourced from Epson Atmix, Japan, where they were produced using a spinning water atomization process (SWAP). The powder composition, measured by inductively coupled plasma optical emission spectroscopy (ICP-OES), consisted of 12.3 ± 1.1 Si, 9.6 ± 0.5 B, 3.0 ± 0.1 Nb, 0.9 ± 0.1 Cu (at%), and a balance of Fe. Examination of the powder morphology using an Apreo 2S microscope (ThermoFisher Scientific) operated at 10 kV, 21 pA, and using a working distance of 3.9 mm, revealed that powder particles have spherical to ellipsoidal shape, with a minor fraction of satellites [52]. The particle size distribution (PSD) was measured using a Bettersizer ST laser analyzer, yielding D_{10}, D_{50}, and D_{90} values of 18, 35, and 58 μm, respectively. The powder flowability, which was assessed using a Hall flowmeter according to standard methods, amounted to 18 s/50 g. The apparent and tapped densities were 3.9 and 4.2 g/cc, respectively. Powders were proved to be 100% amorphous by X-ray diffraction (XRD) in one of our earlier studies [52].

2.2. Laser powder bed fusion processing

Finemet cuboids with dimensions (8 × 8 × 9.5) mm^3 were manufactured by LPBF on a stainless-steel substrate using a Renishaw AM400 pulsed-laser machine, equipped with a reduced build volume (RBV) platform to minimize powder usage. A double scanning strategy, whereby each layer is remelted, was employed to manufacture the parts, as earlier works in similar alloys have suggested that remelting increases densification [59]. This was implemented by assigning two identical STL files to the same XY position, ensuring complete overlap. The fixed process parameters included a hatch distance (h) of 80 μm, a point distance (pd) of 80 μm, a spot size (∅) of 63 μm, and a layer thickness (l_t) of 30 μm. Two LPBF processing conditions, denoted S1 and S2, were investigated. In both cases, the first melting cycle used a laser power (P) of 60 W and a scan speed (v) of 500 mm/s, which had reportedly yielded the highest densification (89%) for this alloy [52], in order to avoid as much as possible the spurious influence of defects. In the second melting cycle, P was kept at 60 W while v was 500 mm/s in sample S1 and 890 mm/s in sample S2, thus covering a significant portion of the narrow LPBF processability window of Finemet [52]. The scan speed was controlled by varying the exposure time (t_{exp}), following the relationship v = pd (μm) / ((t_{exp} + 10)(μs)), where 10 μs is the default time it takes the laser to move between two consecutive spots and thus (t_{exp} + 10)$^{-1}$ is the repetition frequency in μs^{-1}. A meander scanning strategy with a

Table 2
Thermal properties and material parameters employed in the FEM simulations.

Density of bulk material (kg/m^3)	Laser absorptivity		Laser penetration depth (mm)	Interfacial heat transfer coefficient (top domain surface) (W/m^2/°C)	Interfacial heat transfer coefficient (bottom domain surface) (W/m^2/°C)	Latent heat of fusion (J/kg)	Environment temperature (°C)	Solidus Temperature (°C)	Liquidus Temperature (°C)	
7200	0.5		62	50	500	272000	25	1100	1250	
T (°C)	$T \leq T_S$ (solid state)			$T \geq T_L$ (liquid state)						
Heat capacity (J/kg/°C)	527			761						
T (°C)	20	100	200	400	600	800	927	1050	1055	1500
Thermal conductivity (W/m/°C)	73.3	68.2	61.5	48.6	38.9	29.7	29.7	34	33	33

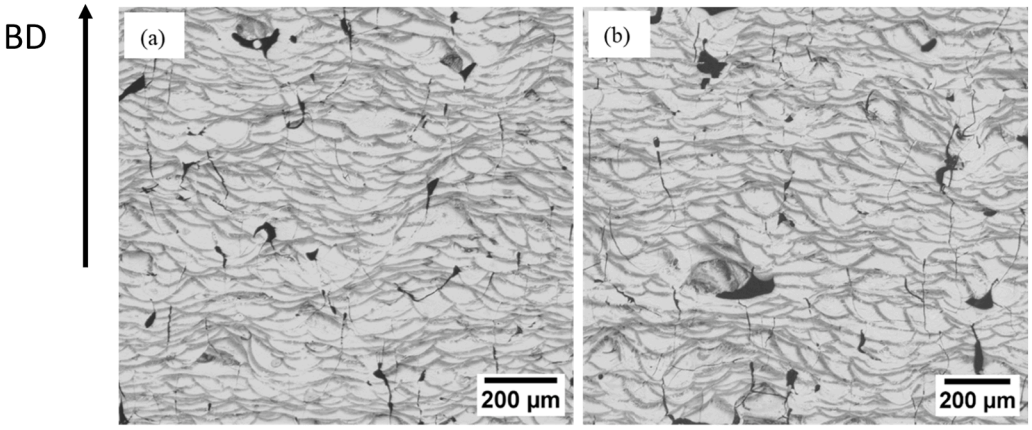

Fig. 1. Optical micrographs illustrating the amorphous/crystalline composite structure of the (a) S1 and (b) S2 etched samples. Crystalline regions surrounding the melt pools are preferentially etched and thus appear as dark gray areas.

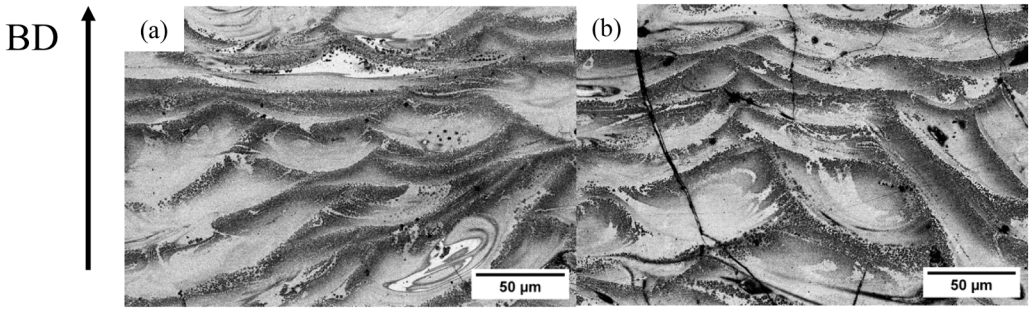

Fig. 2. Representative SEM micrographs illustrating the melt pool structure of (a) S1 and (b) S2 LPBF-manufactured samples. Crystalline regions surrounding the melt pools are preferentially etched and thus appear as dark gray areas. The contrast observed within the melt pool interiors suggests the coexistence of fully amorphous domains (unetched, appearing white) and regions containing varying fractions of crystallites (darker gray tones), which cannot be individually resolved at this magnification.

67° rotation after each layer was employed in the two melting cycles. In short, the first pass was used for densification, while the second scan was tailored to control the (micro)structure, as it was shown earlier that crystallization could be limited by increasing the scan speed [52]. Table 1 summarizes the S1 and S2 LPBF manufacturing conditions, along with the volumetric energy density (VED), corresponding to each melting cycle.

To assess potential differences in the morphology of crystallites formed during solidification versus those originating from devitrification within the heat-affected zone (HAZ), single track-melting was also performed on a fully crystalline, coarse-grained (d = 20 ± 5.6 µm) as-cast Finemet substrate using the same parameters as the second melting cycle in sample S2 (P = 60 W; v = 890 mm/s) (Table 1). Due to the fully crystallized nature of the substrate, devitrification within the HAZ is effectively suppressed. As a result, any crystallization observed can be unambiguously attributed to solidification mechanisms. The cast Finemet substrate was prepared by precisely weighing and melting the elements together in an arc-melting furnace, equipped with a water-cooled copper plate and Ti-gettered Ar atmosphere to prevent oxidation. To ensure the homogeneity of the melt, the ingot was remelted five times after being flipped over.

Finally, in order to prove the effect of the Cu cluster density in the HAZ on the size of the grains nucleating during LPBF, single track-melting was also performed using the same parameters as the second

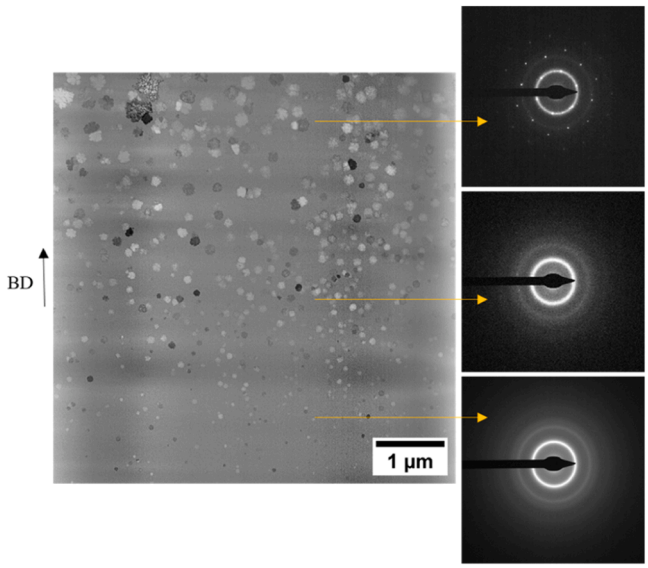

Fig. 3. TEM bright field micrograph illustrating the interior of a selected melt pool in the S1 sample. The SAED patterns included as insets reveal the prevalence of an amorphous phase with locally varying fractions of embedded nanocrystals.

melting cycle in sample S2 (P = 60 W; v = 890 mm/s) on a fully amorphous Finemet substrate produced by induction casting.

2.3. (Micro)structure characterization

Optical microscopy (OM) was performed in all the LPBF-manufactured specimens using an Olympus BX51 microscope at a magnification of 5x to image the defect structure, to measure the density, and to examine the morphology and size of melt pools. The average melt pool depth and width in S1 and S2 conditions were measured by averaging the data from at least 25 melt pools belonging to the last layer of the printed cubes. Sample preparation for OM examination started by sectioning the cuboids at the mid-thickness along the build direction (BD) using a Secotom disc cutting machine. To achieve a mirror-like surface finish, progressive grinding from 320 to 2000 grit SiC papers followed by polishing in three stages with diamond suspensions of 6, 3 and 1 μm was then performed. Revelation of the spatial distribution of the crystalline areas required subsequent etching by immersion for 15–17 s in a standard etchant for Fe-based alloys consisting of 100 ml ethanol (98%), 10 ml nitric acid (65%), and 100 ml distilled water. The IMAGE J/Fiji image analysis software was utilized to segment the bulk material from defects such as cracks and pores [60] and thereby to measure the density. The fraction of the amorphous phase in the LPBF-manufactured specimens was additionally characterized by DSC following a similar procedure to that utilized for the powders, which is explained above in Section 2.1.

SEM examination was performed in the LPBF-processed samples to image the spatial distribution and the morphology of crystallites with an Apreo 2S microscope (ThermoFisher Scientific) and using a backscatter electron (BSE) detector operating with a voltage of 3 kV, a current of 0.2 nA, and a working distance of 4.4 mm. Sample preparation for SEM analysis included the same steps as those described above for OM specimen metallographic surface finishing, along with etching. The (micro)structure of the printed specimens was further examined at higher magnification by transmission electron microscopy (TEM) using a FEI Talos F200x microscope operating at 200 kV. TEM characterization was carried out in the bright field mode, as well as in the scanning transmission (STEM) mode, with a high-angle annular dark field (HAADF) detector. TEM-assisted energy dispersive X-ray spectroscopy (EDX) was used to study the local distribution of alloying elements. To retrieve information on the structure of the crystalline and amorphous phases present, selected area electron diffraction (SAED) patterns were recorded from representative locations along selected zone axes. This technique allows to distinguish Fe(Si) from Fe_3Si phases, which are undistinguishable by XRD. The samples for TEM examination were milled at regions located at the bottom of selected melt pools in S1 and S2 samples using a focused ion beam (FIB) via the trenching-and-lift-out method, as described in the Supplementary Information. As shown in Supplementary Fig. 1a, care was taken to ensure that the lamella was oriented perpendicular to the melt pool perimeter and included a significant portion of both the melt pool interior and the heat-affected zone (HAZ).

2.4. Simulation

In order to understand the role of the scan speed on the (micro) structure during the second pass in S1 and S2 samples, a computational model, based on the finite element method (FEM) [61,62], is used to model the solidification process and during the remelting of a single track. Assuming a conduction mode regime, as indicated by the experimentally observed semi-circular shape of melt pools, in Figs. the model considers the heat transfer and phase transformation physics coupled to each other. The temperature evolution in the LPBF-manufactured Finemet part, during the additive manufacturing process, is computed by solving the following heat transfer equation:

$$\rho c_p \frac{\partial T}{\partial t} = \nabla \bullet (k \nabla T) + Q_l + Q_\phi, \tag{1}$$

where ρ is the density, c_p is the specific heat capacity, T is the temperature, t is the time, k is the isotropic conductivity, and Q_l and Q_ϕ are heat due to the laser incidence and phase change (melting/solidification), respectively. Normal heat flux (q_c) boundary conditions are applied using Newton's law, $q_c = -h_c(T - T_\infty)$, where h_c is the interfacial heat transfer coefficient and T_∞ is the environment temperature.

The pulsed laser is modeled by successive steps consisting of laser activation, laser deactivation, and laser movement. When the laser is on, the heat term Q_l is computed by means of the following Gaussian-based source [63]:

$$Q_l = \alpha_p \frac{G_l I_z}{H_l}, \tag{2}$$

where α_p is the laser absorptivity, $G_l = \frac{2P}{\pi \varnothing^2} \exp\left(-2 \frac{(x-x_l)^2 + (y-y_l)^2}{\varnothing^2} \right)$ is the Gaussian distribution at the irradiated surface, P is the laser power, $\varnothing$ is the laser diameter, $I_z = \frac{1}{0.75}\left[-2.25\left(\frac{z_l - z}{H_l}\right)^2 + 1.5\left(\frac{z_l - z}{H_l}\right) + 0.75 \right]$ is a parabolic decay to consider the laser penetration, and H_l is the laser penetration depth. The laser movement is defined with respect to the Cartesian coordinate system (x, y, z), where (x_l, y_l, z_l) are the coordinates of center of the laser spot that irradiates the surface placed at z_l.

The heat released/absorbed due to solid/liquid phase transformations (Q_ϕ) is computed as $Q_\phi = \rho L_f \frac{\partial f_s}{\partial t}$, where L_f is the latent heat of fusion and f_s is the solid volume fraction. To address the evolution of solid volume fraction f_s, the previously described thermal model is coupled with a simple metallurgical model. The latter considers that when the temperature of the bulk exceeds the liquidus temperature (T_L), the solid is completely transformed into a liquid phase ($f_s = 0$). In turn, when the temperature of the liquid phase falls below the solidus temperature (T_S), the liquid is completely transformed into a solid ($f_s = 1$). A linear variation of f_s with T is used between T_L and T_S.

The equations are solved into the whole part geometry by using the Abaqus finite element software. The coupling between the thermal and metallurgical models is programmed by means Abaqus user defined Fortran subroutines. The temperature evolution in the HAZ and the

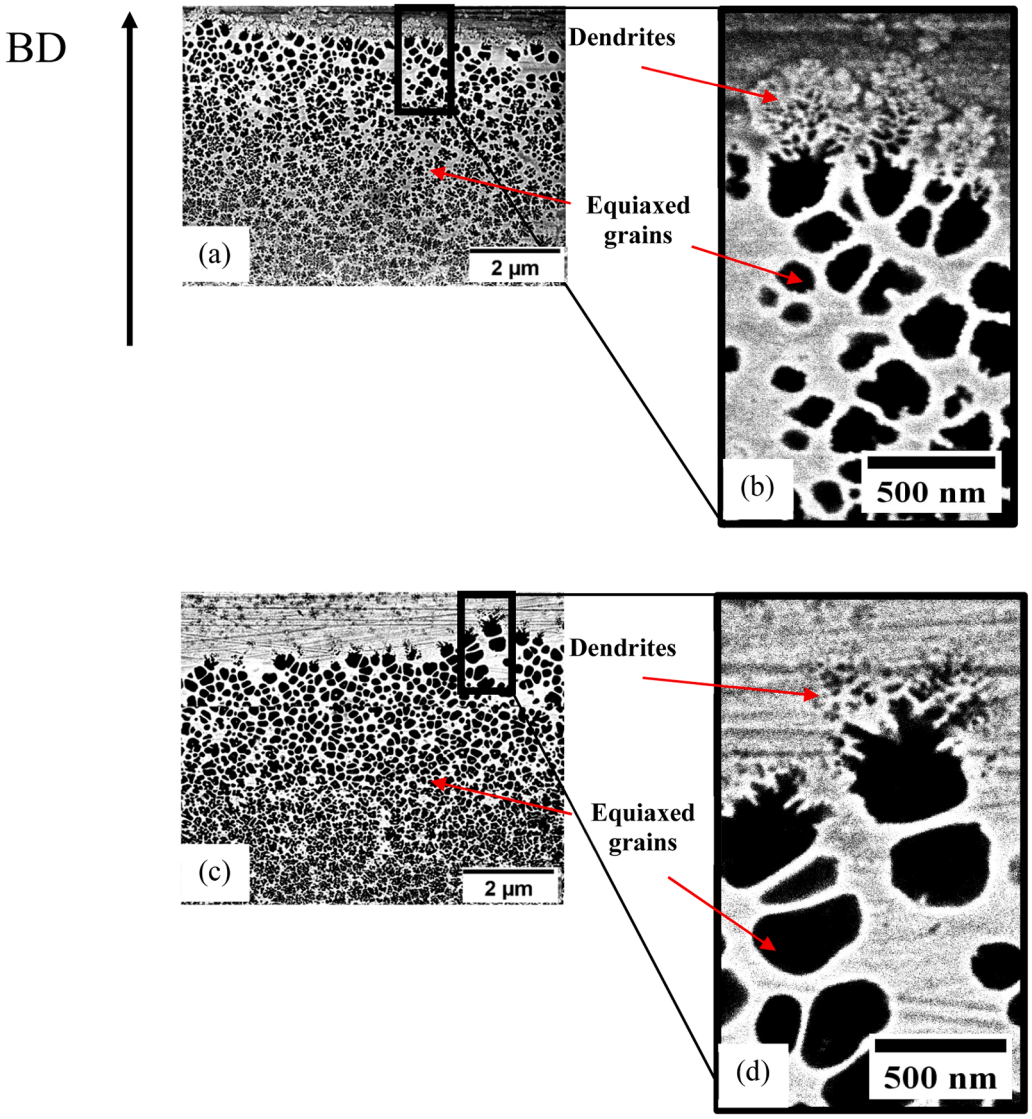

Fig. 4. Representative SEM micrographs illustrating the crystalline region surrounding a selected melt pool at different magnifications in the LPBF-manufactured (a, b) S1 and (c,d) S2 etched samples. Crystallites are preferentially etched, and they thus appear as dark regions.

temperature/cooling rate fields in the melt pool are extracted directly from Abaqus software. The liquid-solid interface velocity during solidification was computed by postprocessing FEM results, using an in-house Matlab/Octave code to track the interface positions over time.

The physical properties employed in the simulations are summarized in Table 2. ρ, c_p, and L_f were taken from the Fe-based Kuamet 6B2 alloy [62] due to the lack of data on Finemet and to the similarity in their chemical composition. T_S and T_L were obtained from differential scanning calorimetry (DSC) measurements. The thermal conductivity (k) of pure Fe was utilized because there is lack of data on Finemet [64]. h_c is defined according to the surface from which heat is extracted (top and bottom) as in [61]. Finally, the laser parameters α_p and H_l are obtained by calibration to have a good match between the experimental and simulated melt pool sizes.

3. Results

The composition of the LPBF-manufactured samples, measured by ICP-OES, consisted of 12.8 ± 1.1 Si, 8.6 ± 0.5 B, 2.8 ± 0.1 Nb, 0.90 ± 0.08 Cu, Fe-balance (at%) for S1, and 13.1 Si, 8.8 B, 3.0 Nb, 1.0 Cu, Fe-balance (at%) for S2. Both compositions are very similar to that of the original powders (see Section 2), although with a slightly lower content of B, that might have evaporated during processing. LPBF of the Finemet alloy under the S1 and S2 conditions examined in this study results in the formation of amorphous/crystalline composites, as illustrated in Fig. 1. Representative etched cross-sections parallel to BD for samples S1 (Fig. 1a) and S2 (Fig. 1b) reveal distinct microstructural features. Crystalline regions surrounding the melt pool circumference are preferentially etched and appear dark in the micrographs, whereas areas with a high amorphous phase content resist etching and thus appear lighter. The meander scanning strategy with 67° interlayer rotation leads to variations in melt pool shape and size along BD. It must be emphasized here that, nevertheless, the semicircular morphology of the melt pools confirms that melting occurred in conduction mode. The melt pool dimensions were measured at the top layer. The average melt pool width is 103 ± 7 μm in S1 and 80 ± 6 μm in S2, with corresponding depths of 36 ± 3 μm and 28 ± 6 μm, respectively. The manufactured samples exhibit relative densities of 94% for S1 and 92% for S2 with amorphous phase fractions of 23% and 27%, respectively.

Fig. 2 presents SEM micrographs offering a more detailed view of the melt pool structure on etched surfaces of the S1 (Fig. 2a) and S2 (Fig. 2b) LPBF-manufactured samples. Consistent with the observations in Fig. 1, the crystalline regions, appearing dark gray due to preferential etching, are primarily located around the melt pool peripheries. The presence of

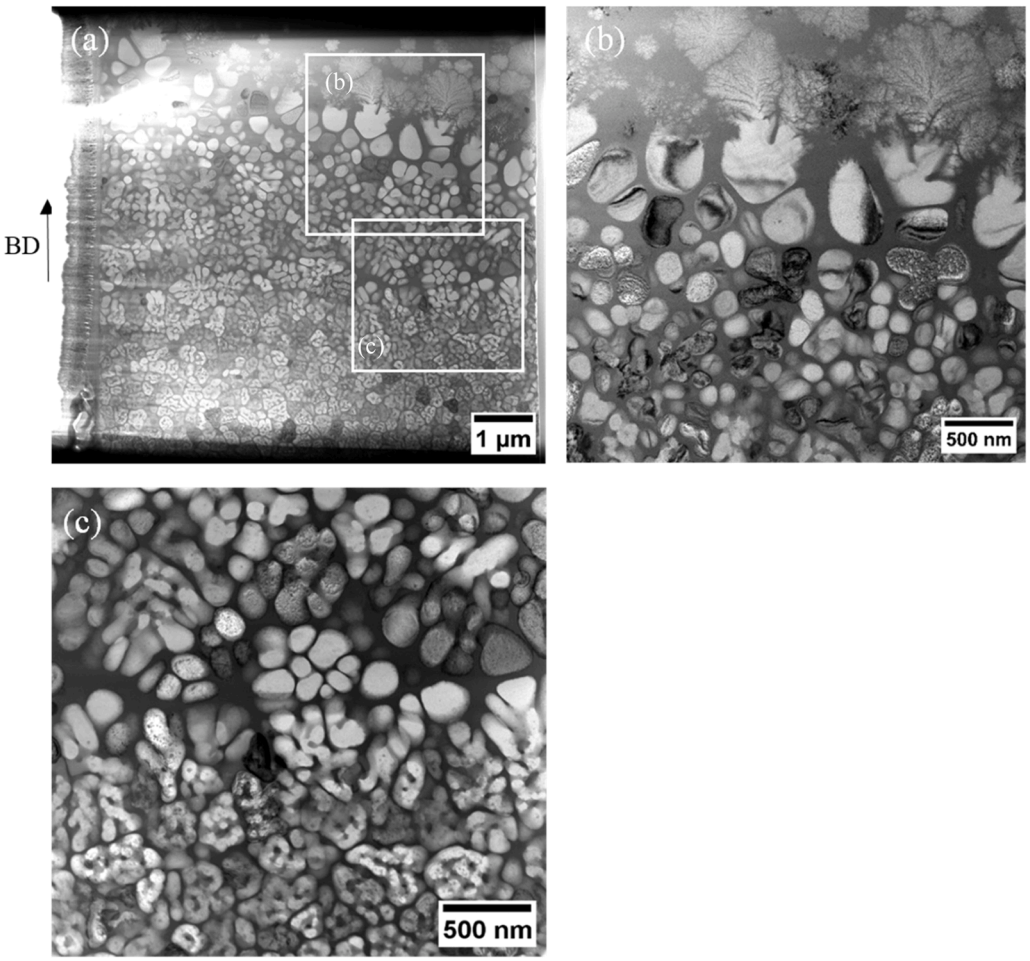

Fig. 5. Bright field TEM micrographs illustrating the crystalline region in the vicinity of a representative melt pool in sample S1 at different magnifications. (a) Overview of the entire TEM lamella; (b,c) high magnification images of the areas which are indicated in (a) using white rectangles.

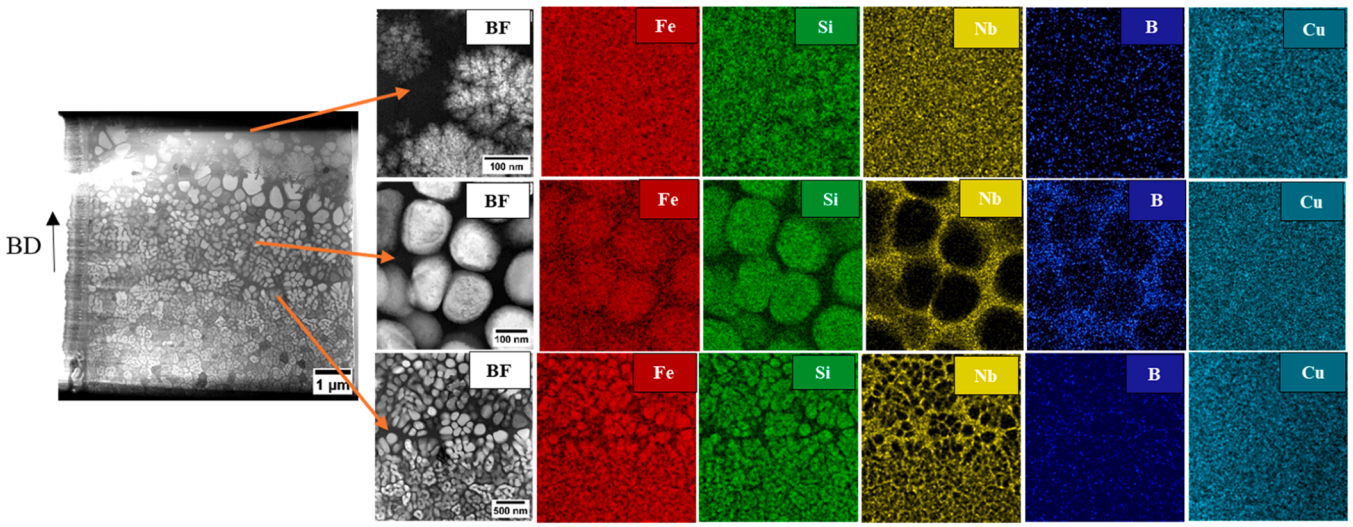

Fig. 6. TEM EDX elemental maps corresponding to different locations of within the crystalline area of sample S1 depicted in Fig. 5a, which is included here also for reference.

nearby cracks and pores (Fig. 2b) traversing some melt pools does not appear to have any influence in the microstructure of their surrounding crystalline regions. Within the interiors of the melt pools, SEM analysis reveals areas of varying gray tones, indicative of a heterogeneous microstructure. The lighter regions, highly resistant to etching, correspond to fully amorphous domains, while the darker gray areas suggest regions with increasing fractions of crystallites. Although individual nanocrystals are not resolvable at this magnification, their presence is

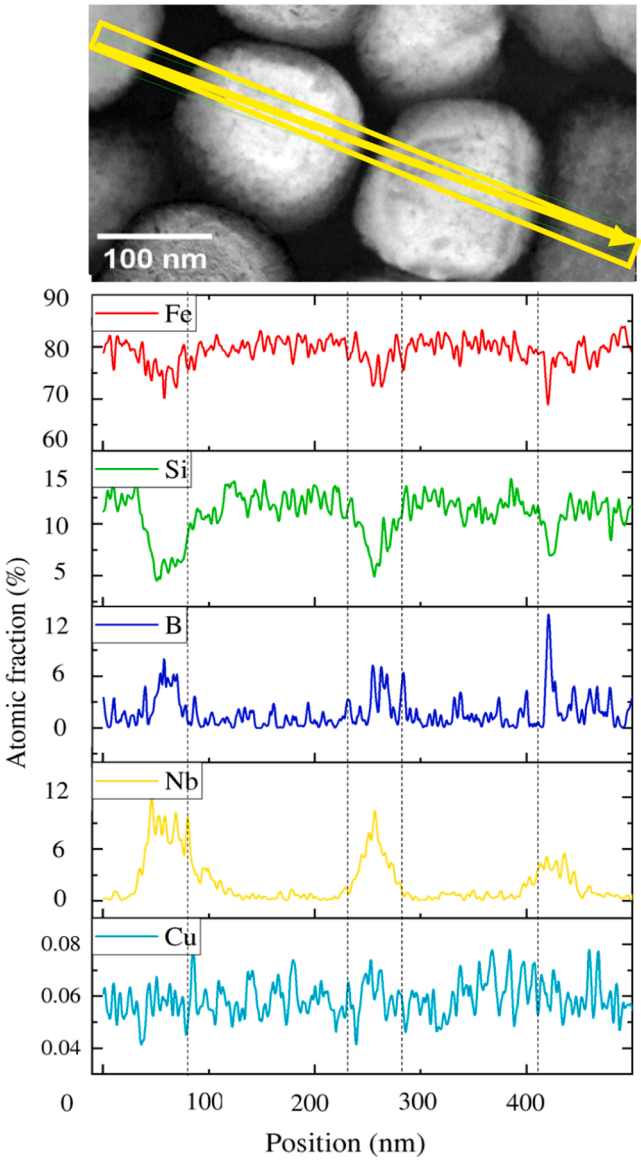

Fig. 7. TEM EDX elemental composition line profiles along the path indicated in the TEM micrograph above. The investigated region is located within the area populated by equiaxed grains in the S1 sample depicted in Fig. 5a.

inferred from the contrast developed upon etching. Fig. 3 shows a representative high-magnification TEM bright-field image of a melt pool interior in sample S1. The accompanying SAED patterns confirm the presence of an amorphous matrix interspersed with nanocrystalline domains.

SEM was further employed to investigate the crystalline regions at the bottom of melt pools in greater detail. Fig. 4 shows several SEM micrographs at different magnifications for the S1 (Figs. 4a, b) and S2 (Fig. 4c, d) specimens. In both cases, the top layer of the crystalline region is composed of dendritic grains growing approximately perpendicular to the melt pool boundary. The remaining crystallites—which represent the vast majority—exhibit an equiaxed morphology. Dendritic and equiaxed crystals are highlighted in Fig. 4 using arrows. As shown in the high-magnification images in Figs. 4b and 4d, dendritic grains are noticeably longer in the S1 sample compared to the S2 specimen. Equiaxed grains exhibit sizes ranging from tens of nm up to 400 nm in diameter, i.e., their size distribution is much broader than that resulting from isothermal annealing of melt-spun ribbons, which usually have diameters of approximately 10–20 nm [28]. In both samples, on average, the size of the equiaxed grains decreases as the distance with respect to the bottom of the melt pool increases.

In the following TEM will be utilized to examine in greater detail the morphology, the local chemical composition, and the structure of the crystalline regions surrounding melt pools in samples S1 (Figs. 5–8) and S2 (Fig. 9–12) in order to determine whether the LPBF processing parameters and, in particular, the increase in scan speed during the second melting cycle (500 mm/s in S1 vs. 890 mm/s in S2), has any influence on the nature of the crystallites. Fig. 5 presents a series of bright-field TEM micrographs that illustrate the grain morphology in a representative crystalline region of the S1 sample. Fig. 5a depicts the entire FIB-milled TEM lamella, which was cut perpendicular to the melt pool circumference as shown in Supplementary Figure 1a, while Fig. 5b,c provide detailed views of the microstructure: dendritic grains growing perpendicular to the melt pool perimeter at the top layer (Fig. 5b), and equiaxed grains located immediately beneath them (Fig. 5c). These observations corroborate the features highlighted in Fig. 4, while further revealing that the dendritic grains consist of very fine arms, each less than 100 nm thick, and reach heights of approximately 500–700 nm.

Fig. 6 presents TEM-EDX elemental maps of Fe, Si, Nb, B, and Cu across the region shown in Fig. 5a, providing insight into the local chemical distribution. Cu appears uniformly distributed throughout the area. Although atomic-scale Cu clustering is frequently reported in melt-spun Finemet ribbons and is known to play a role in crystallization during isothermal annealing [28], the spatial resolution of the current TEM-EDX setup is insufficient to detect such clustering directly. Nonetheless, its presence cannot be definitively ruled out. All crystallites are primarily composed of Fe and Si, consistent with the nanograins typically observed during isothermal annealing of melt-spun ribbons [28]. Finally, clear partitioning of Nb and B into the amorphous matrix is evident in regions containing equiaxed crystallites. However, the limited resolution of the TEM-EDX technique precludes determining whether a similar elemental partitioning occurs within the dendritic zones near the top layer.

Fig. 7 shows a representative TEM-EDX line profile acquired across several equiaxed grains in sample S1. In line with the elemental maps in Fig. 6, crystallites are enriched in Si and Fe, while the surrounding amorphous phase contains higher levels of Nb and B. For each element, the local concentration was estimated as the maximum value recorded across the line profile. Seven grains were analyzed to determine the average content of different elements in the crystalline phase, and the surrounding amorphous regions were evaluated to estimate the average content of alloying elements in the glassy phase. Due to its low atomic number, accurate quantification of B was not possible with the employed technique. The average Si contents in the grains and in the surrounding amorphous fraction are 13.8 ± 0.5 at% and 6.6 ± 1.1 at%, respectively. The former exceeds slightly the nominal composition of 12.8 at%, while, as expected, the latter falls below it. The average Nb contents in the crystals and the surrounding amorphous fraction are, respectively, 0.9 ± 0.7 at% and 9.0 ± 1.5 at%. When compared with the nominal composition of 2.8 at%, these data confirm an almost complete Nb partitioning into the amorphous regions.

Fig. 8 presents a collection of $< 110 >$ TEM SAED patterns illustrating the structure of the crystallites at different locations within the area of sample S1 depicted in Fig. 5a, which is included in the figure also for reference. Fig. 8a reveals that the dendritic grains growing perpendicular to the melt pool diameter at the top layer have a DO_3 structure. The white circles highlight the reflections that would correspond to an α (disordered) phase, in which Si would be in solid solution, and the red circles highlight the extra superlattice reflections that denote the presence of the ordered DO_3 structure. Fig. 8b,c confirm that equiaxed grains at the remaining two investigated locations also possess a DO_3 structure. The green circles indicate weak reflections that correspond to extinctions. The origin of the visibility of these spots is probably related to dynamic scattering effects related to local variations in the sample thickness. The stabilization of an ordered DO_3 structure agrees with the

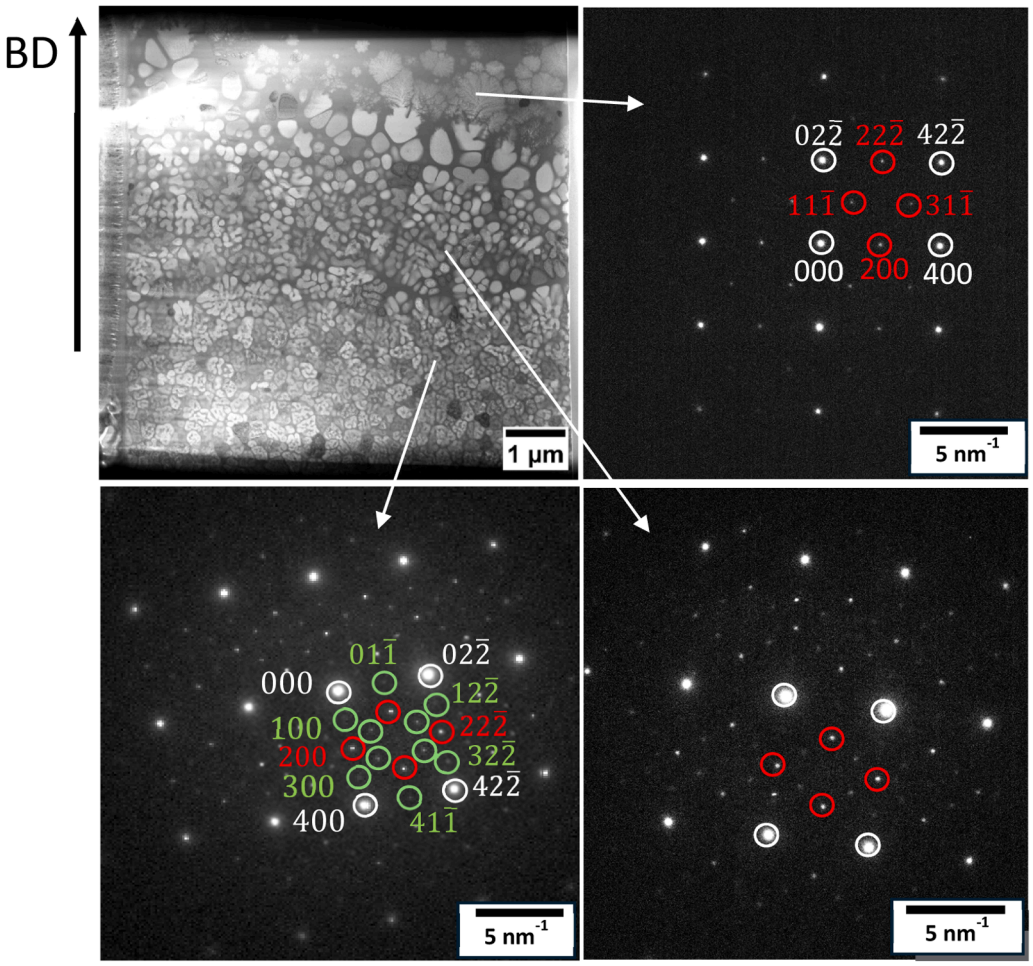

Fig. 8. < 110 > TEM SAED patterns illustrating the structure of the crystallites at different locations within the area of sample S1 depicted in Fig. 6a, which is included here also for reference. (a) Dendritic grains growing perpendicular to the melt pool perimeter; (b,c) equiaxed grains. The white circles highlight the reflections corresponding to the α (disordered) phase, the red circles correspond to extra superlattice reflections that reveal the presence of an ordered DO_3 structure, and the green circles highlight additional DO_3 superlattice reflections, which are usually extinct.

Fe-Si equilibrium phase diagram for an atomic concentration of Si of approximately 13% [65], as well as with earlier observations of nanocrystallization in Finemet during isothermal annealing treatments [66].

Supplementary Figs. 2–5 show representative micrographs at different magnifications of the spatial distribution and microstructure of the crystalline regions in a specimen manufactured using the same LPBF processing parameters as sample S1 but employing a single melting cycle per layer. Comparison of Supplementary Figs. 2–5 with Figs. 1a, 2a, 3a, 5, 6, and 8 reveals a high degree of similarity in the crystalline microstructures of the two samples. This agreement confirms that the use of double melting is appropriate for the present study, as it increases density without altering the underlying crystallization mechanisms.

Fig. 9 presents a series of bright-field TEM micrographs depicting the grain morphology within a representative crystalline region of the S2 sample. Fig. 9a shows the entire FIB-milled TEM lamella, extracted perpendicular to the melt pool circumference, as indicated in Fig. 1a. Higher-magnification views are provided in Fig. 9b–d: Fig. 9b highlights dendritic grains growing perpendicular to the melt pool perimeter at the top layer, while Figs. 9c and 9d reveal the equiaxed grains located immediately beneath, as also observed in sample S1. The dendritic crystallites are composed of fine arms less than 100 nm thick and exhibit an overall length of approximately 200 nm—significantly smaller than their counterparts in the S1 sample, which ranged from 500 to 700 nm in length.

Fig. 10 presents TEM-EDX elemental maps of Fe, Si, Nb, B, and Cu across the region shown in Fig. 9a, providing insight into the local chemical distribution. The local composition is very similar to that found in S1. In short, Cu appears uniformly distributed throughout the examined area, all crystallites are primarily composed of Fe and Si, and Nb and B partition to the amorphous matrix. Fig. 11 shows a representative TEM-EDX line profile acquired across several equiaxed grains in sample S2. Six grains and their surrounding amorphous regions were evaluated. The average Si contents in the crystallites and in the glassy phase are, respectively, 12.9 ± 0.9 at% and 7.7 ± 1.2 at%, i.e., similar to those found in S1 (Fig. 7). The average Nb contents in the crystallites and the surrounding amorphous fraction are, respectively, 0.7 ± 0.4 at % and 8.0 ± 1.0 at%, confirming an almost complete Nb partitioning into the amorphous regions also in S2.

Fig. 12 depicts a collection of < 110 > TEM SAED patterns illustrating the structure of the equiaxed crystallites at different locations within the area of sample S2 depicted in Fig. 9a, which is included in the figure also for reference. It was unfortunately not possible to capture an SAED pattern of the dendritic grains located at the top due to their small size. Fig. 12 shows that, irrespective of their location within the crystalline region, all equiaxed grains have a DO_3 structure. A detailed indexing of the DO_3 superlattice reflections can be found in Fig. 8.

To determine whether the dendritic and equiaxed grains observed in samples S1 and S2 form by solidification of the molten region or via devitrification in the heat-affected zone (HAZ), single-track melting experiments were conducted using identical LPBF conditions on two

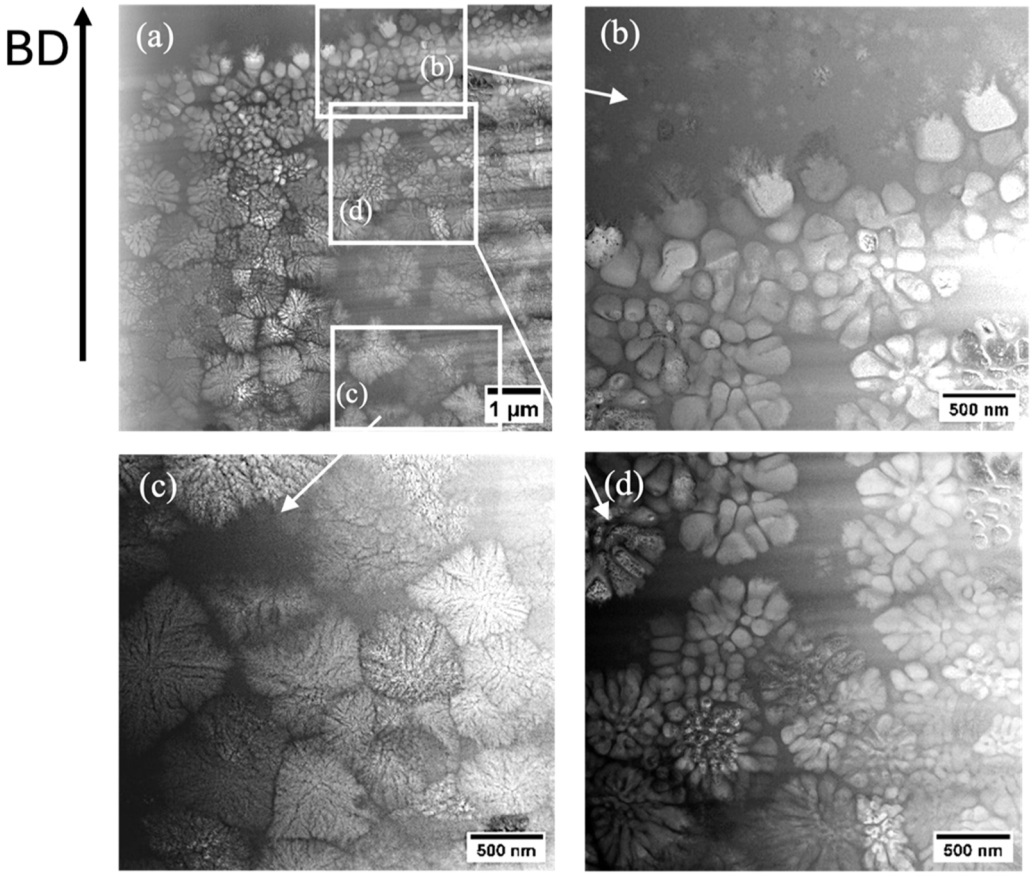

Fig. 9. Bright field TEM micrographs illustrating the crystalline region in the vicinity of a representative melt pool in sample S2 at different magnifications. (a) Overview of the entire TEM lamella; (b-d) high magnification images of the areas which are indicated in (a) using rectangles.

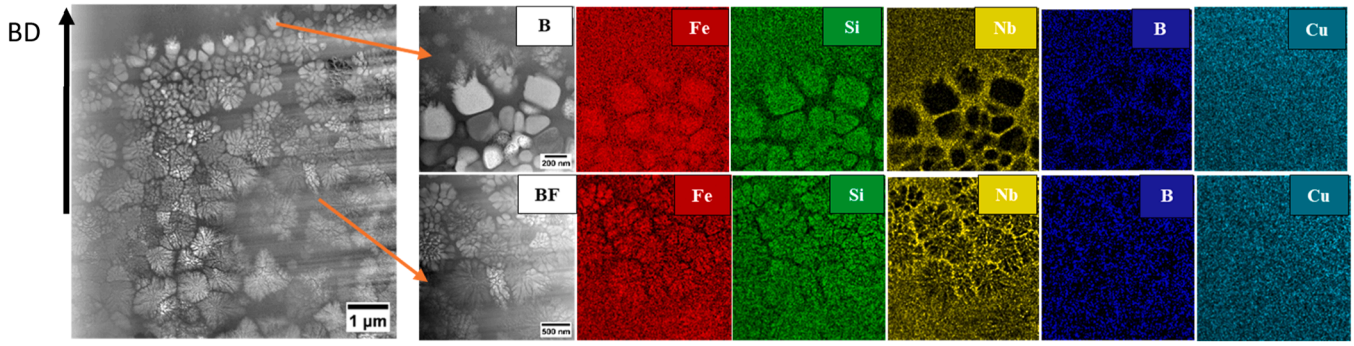

Fig. 10. TEM EDX elemental maps corresponding to different locations within the crystalline area of sample S2 depicted in Fig. 10a, which is included here also for reference.

substrates: a fully crystalline, coarse-grained (d = 20 ± 5.6 μm) as-cast Finemet® substrate (Figs. 13 and 14), and a fully amorphous Finemet® substrate (Fig. 15), produced by induction casting. In both cases the processing parameters matched those of the second melting pass used for sample S2 (P = 60 W; v = 890 mm/s) (Table 1). In the crystalline substrate the only possible way for new crystals to form is during solidification of the melt pool. Fig. 13a,b show images of the single scan track along two perpendicular planes. Fig. 13b clearly reveals the characteristic semicircular melt pool embedded in the crystalline matrix. A TEM lamella was extracted via FIB milling from the bottom of this melt pool as shown in Fig. 14a to investigate whether there were any crystals that formed during solidification. Fig. 14b reveals, indeed, that only DO_3 dendritic grains, similar to those observed at the top layer of crystalline regions in samples S1 (Fig. 5) and S2 (Fig. 9), grow perpendicular to the melt pool perimeter. Fig. 15 illustrates an SEM micrograph of a cross section of the single track melted on the amorphous substrate. Here, dendritic grains are also observed at the bottom of the melt pool but, additionally, a high density of equiaxed grains populate the HAZ. Consequently, we attribute the dendritic grains in S1 and S2 to crystallization during solidification, and the equiaxed grains to devitrification and subsequent grain growth mechanisms.

4. Discussion

4.1. Effect of the laser scan rate on the formation of crystallites during solidification

Our results confirm that crystal formation during LPBF in Finemet

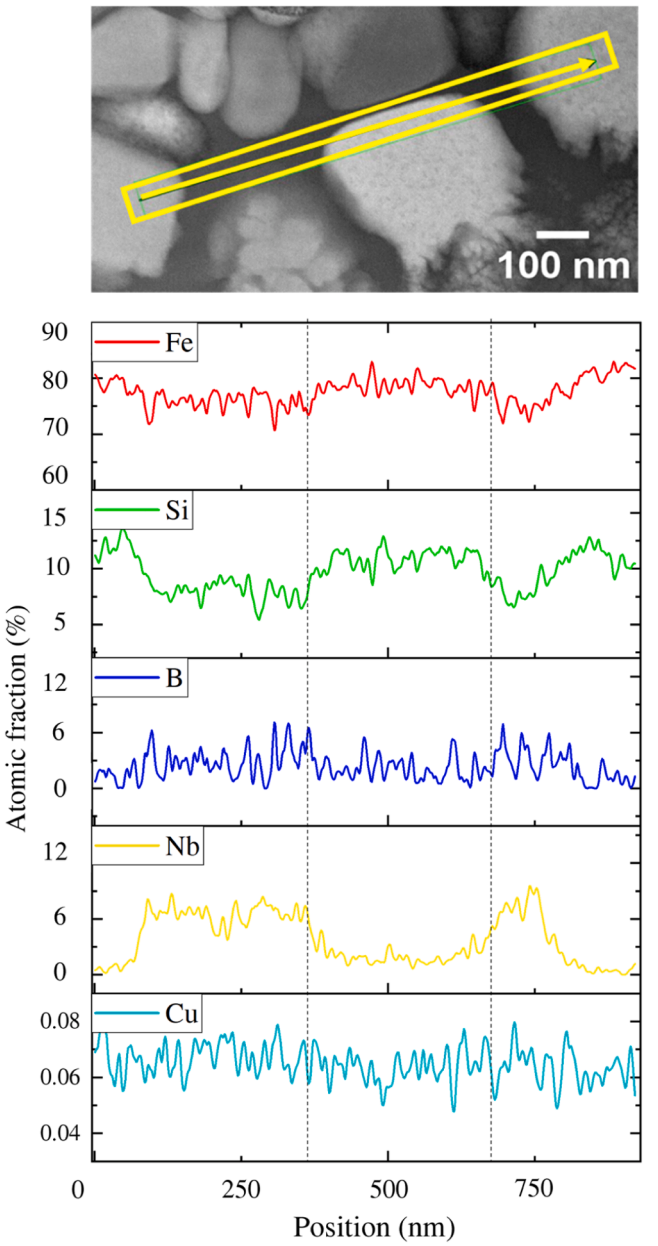

Fig. 11. TEM EDX elemental composition line profiles along the path indicated in the TEM micrograph above. The line traverses several equiaxed grains in the S2 sample.

takes place mostly by devitrification in the HAZ of the glassy layer underneath the melt pool, in agreement with other BMG studies [42,58,67–70]. However, we show clear evidence that a thin crystalline layer of dendritic morphology with a growth direction parallel to the BD also forms at the edges of melt pools during solidification. Crystallization during solidification was also reported in an earlier SEM study by Li et al. [71] on LPBF of another glass forming system (Al-based) with similarly low glass forming ability and with composition Al86Ni6Y4.5Co2La1.5 (at%).

Comparison of Figs. 5b and 9b reveals that increasing the laser scan speed leads to the formation of smaller dendritic crystals during solidification. In the following, we use FEM modeling to simulate the solidification process in a single track printed over a solid substrate with the processing parameters corresponding to the second pass in S1 and S2 samples. Fig. 16 illustrates the variation of the solid/liquid interface velocity (Fig. 16a), the temperature gradient at the interface (Fig. 16b), and the cooling rate at the interface (Fig. 16c) as a function of the solid/liquid interface position along the path indicated by the white dotted lines in Fig. 16d (S1) and 16e (S2). The coloring in Figs. 16d and 16e indicates the maximum temperature (in °C) reached within each melt pool during the solidification process. Fig. 16 reveals that, as the solidification process proceeds, i.e., as the interface moves toward the top of the layer, the interface velocity increases and the temperature gradient at the interface decreases. The depth of the S1 and S2 melt pools can be estimated from Fig. 16a to be ~43 and ~30 μm, respectively, which is in good agreement with the experimental measurements (36 ± 3 μm and 28 ± 6 μm, for S1 and S2, respectively). Fig. 16c confirms that the cooling rate is lower in the S1 sample than in the S2 specimen. In particular, the cooling rates at the bottom of the corresponding melt pools are, respectively, 8.5×10^6 and 1.3×10^7 °C/s. The smaller size of the solidified crystals in S2 can thus be attributed to the faster cooling rate in this specimen.

4.2. *Devitrification during laser powder bed fusion*

Devitrification in the HAZ of S1 and S2 samples leads to the formation of equiaxed grains (Figs. 5 and 9). The observed elemental partitioning in the equiaxed grains, where crystallites exhibit a higher Si concentration than the surrounding amorphous regions and are fully depleted of Nb and B, supports the conclusion that these grains form via primary crystallization. This mechanism has been widely reported during isothermal annealing of melt-spun Finemet ribbons, typically conducted at 550 °C for 60 min, which results in the formation of a nanocrystalline microstructure with grain sizes of ~10–20 nm, a condition associated with optimal soft magnetic performance [28].

The stabilization of Fe-Si nanograins during isothermal annealing has been attributed to a combination of heterogeneous nucleation at Cu atom clusters (~5 nm in size) and to the sluggish movement of grain boundaries due to the presence of Nb in solid solution in the amorphous matrix, that prevents grain coarsening [29,66,72,73]. Cu clusters are, for the most part, formed already during quenching. Indeed, cluster densities of approximately 10^{24} m^{-3}, which are of the same order of magnitude as the number of 10–20 nm-sized crystallites formed during optimum heat treatment conditions, have been reported in the as-spun state [30].

Our results demonstrate that the size distribution of the grains formed by devitrification in the HAZ of LPBF-processed specimens is significantly broader than that observed in isothermally annealed melt-spun ribbons. In particular, grains in the vicinity of the melt pools are ~400 nm in size, and the grain size decreases progressively with the distance to the melt pool down to a few tens of nanometers. In the following we rationalize the formation of this gradient crystalline structure in the HAZ on the light of the classical nucleation and growth theory of crystals [74].

4.2.1. *Nucleation*

The density of grains in the S1 and S2 samples, estimated from the TEM micrographs of Figs. 5 and 9, is on average roughly of the order of 10^{19} m^{-3}, i.e., about five orders of magnitude smaller than that present in the melt-spun ribbons that are isothermally annealed at T~550°C. As shown in Figs. 4, 5, and 9, the grains formed by devitrification, irrespective of their size, remain fully embedded in the amorphous matrix and they do not impinge on each other. Thus, the lower density of devitrified grains observed in the LPBF-manufactured specimens reveals that the density of the Cu clusters, which are undetectable within the resolution limits of our TEM, is also reduced in LPBF-processed specimens compared to melt-spun ribbons. In the following we examine whether the smaller Cu cluster density in the 3D printed specimens could be attributed to the presence of higher cooling rates, which would restrict short-range diffusion during solidification.

Earlier works have reported that cooling rates during melt-spinning of Fe-based amorphous ribbons might range from 4.0×10^4–6.9×10^6

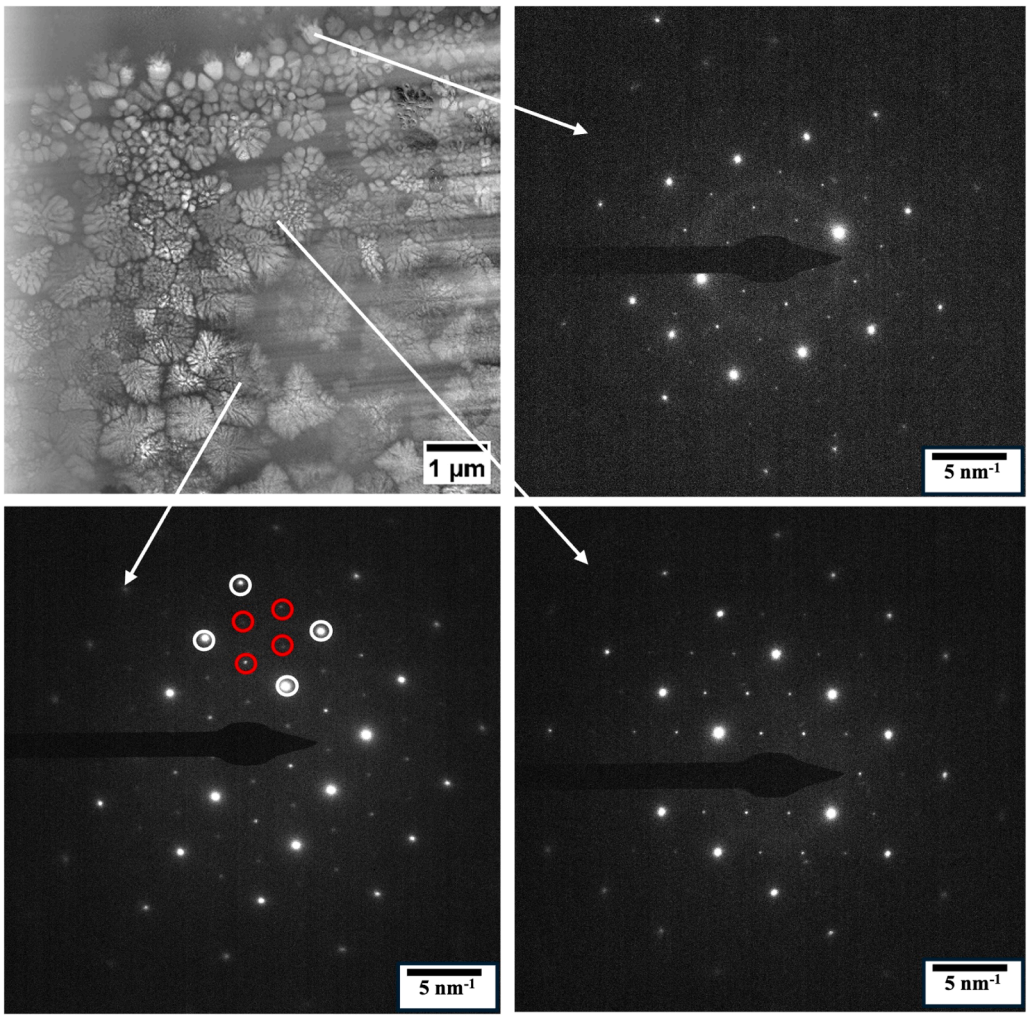

Fig. 12. < 110 > TEM SAED patterns illustrating the structure of the equiaxed crystallites at different locations within the area of sample S2 depicted in Fig. 9a, which is included here also for reference. The white circles highlight the reflections corresponding to the Fe(Si) (disordered) phase, and the red circles correspond to extra superlattice reflections that reveal the presence of an ordered DO_3 structure.

°C/s as a function mainly of the wheel speed [75]. In general, isothermal annealing studies in Finemet are carried out in relatively thin ribbons, with thicknesses between 20 and 30 μm [26,66,76], produced at wheel speeds between 25 and 30 m/s. These conditions correspond to cooling rates of approximately 5×10^5 and 3×10^6 °C/s [75], with variations within this range attributed to other processing parameters, such as the gas ejection pressure and the melt ejection temperature, which are seldom reported in the literature. As shown in Fig. 16c, the LPBF cooling rates along the path indicated in Figs. 16d and 16e (white dotted lines) are consistently higher than those corresponding to melt spinning. In particular, in the S1 sample cooling rates range from 4.8×10^6 (interface position= 2 μm) and 8.5×10^6 °C/s (interface position= 41 μm) and in the S2 sample cooling rates range from 8.3×10^6 (interface position= 7 μm) and 1.3×10^7 °C/s (interface position= 29 μm). These higher cooling rates in LPBF process might account for the reduced density of Cu clusters and, thus, for the lower number of devitrified crystallites. (A note must be made here that we are not considering the influence of the shear rate during the melt spinning process, which further promotes nucleation [77,78]).

4.2.2. Growth

The lack of coalescence of the grains formed by devitrification is attributed to the substantial Nb content retained in the amorphous phase (~9 at% in S1 and ~8 at% in S2), which is comparable to that reported earlier for isothermally annealed ribbons (10 at% [30]). Given this similarity in the Nb content, the lattice resistance to the grain boundary movement should be similar in LPBF-specimens and in melt-spun ribbons. Thus, the drastically more pronounced grain growth in the 3D printed specimens must be attributed to more extreme thermal conditions during the intrinsic heat treatment associated to LPBF processing. Fig. 17 illustrates the FEM-simulated temperature profiles at different locations within the HAZ in the vicinity of the melt pool boundary in the S1 (Fig. 17a) and S2 (Fig. 17b) samples. In particular, the profiles were simulated at positions located at a distance from the top of the melt pool of 46.8, 50.9, and 56.1 μm in S1 (Fig. 17a) and of 30.7, 35.2, and 40.4 μm in S2 (Fig. 17b). As expected, at a given instant of time, the temperature of the intrinsic heat treatment in both samples decreases as the distance to the melt pool increases. Additionally, the maximum temperatures, in the range of 800–900–1100°C, are significantly higher than the Fe-Si crystallization temperature observed when applying a typical DSC heating scan rate of 20 °C/s (T_x=540°C-550°C) and, indeed, approach the solidus temperature (T_S=1100°C). It is our contention that even a short period of time (Δt~0.2–0.4 ms) (Fig. 17a,b) at such extreme temperatures leads to the observed grain growth in the HAZ of S1 and S2 samples (Figs. 5 and 9).

Fig. 18 illustrates schematically the origin of gradient crystalline structure in the HAZ of the S1 and S2 LPBF-manufactured samples as interpreted from the classical nucleation and growth theory [79]. In

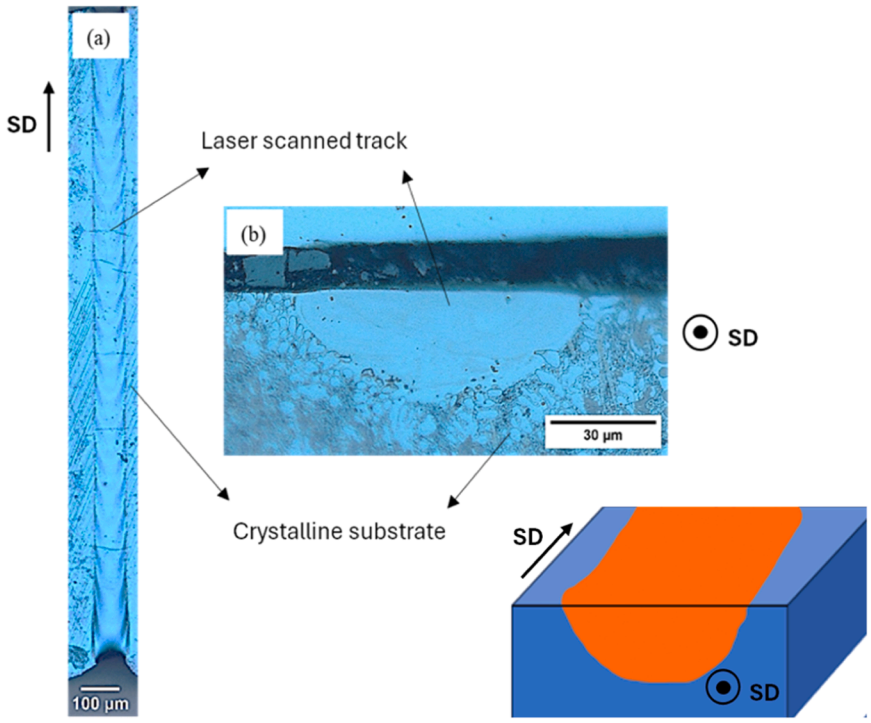

Fig. 13. Image of the single scan performed on the fully crystallized Finemet substrate along two perpendicular planes. (a) Optical micrograph captured along a plane parallel to the scan direction (SD); (b) SEM image obtained along a plane perpendicular to SD. A 3D schematic showing the two planes of observation is included for further clarity.

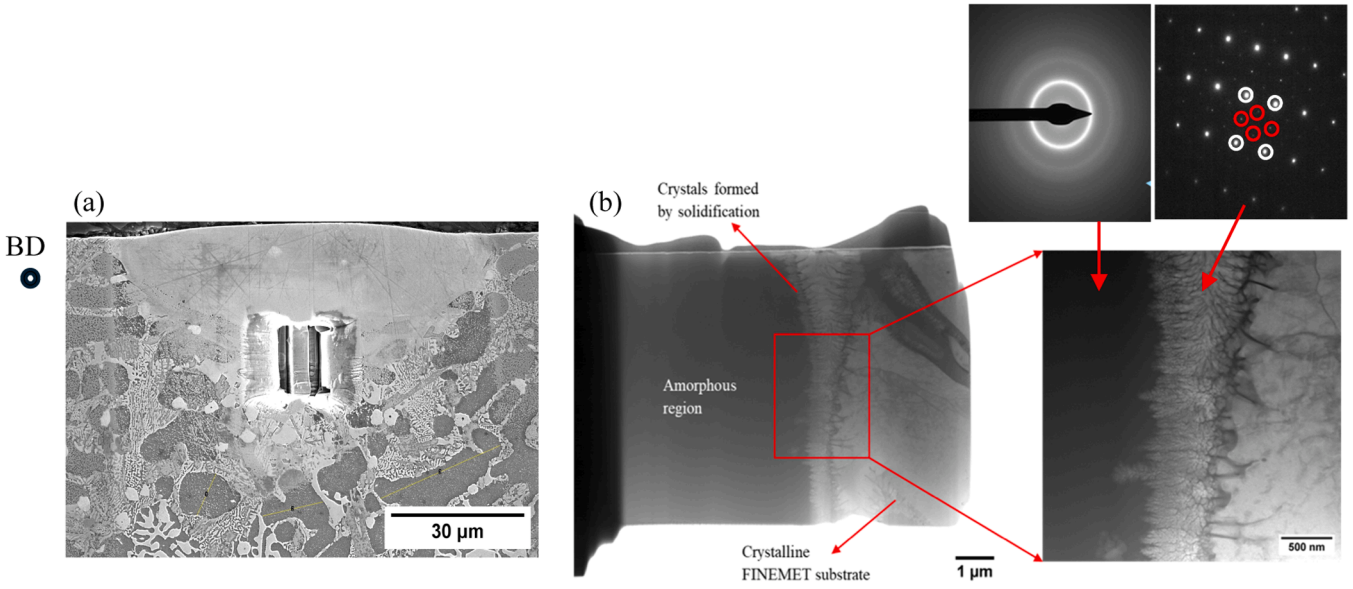

Fig. 14. (a) SEM image of a cross section of the single track perpendicular to SD highlighting the location where the TEM lamella was FIB-milled; (b) Two TEM bright field micrographs at different magnifications illustrating the dendritic morphology of the crystallites formed during solidification. The SAED patterns included as insets correspond to the amorphous phase (ring pattern) and to the DO_3 structure (<110 > zone axis) of the dendritic grains. The white and red circles indicate DO_3 reflections.

particular, Fig. 18 plots the growth rate ($\dot{G}$, green line) and the nucleation rate ($\dot{N}$, blue line) with respect to the local in-situ heat treatment temperature for the transformation of devitrification from the previously deposited amorphous phase. In regions right next to the melt pool boundary, the nucleation rate is very small and the growth rate is large, thus leading to large grains. In turn, as the distance to the melt pool boundary increases, $\dot{N}$ increases and $\dot{G}$ decreases, and thus the in-situ heat treatment results in larger number of smaller grains.

In comparison with the LPBF-manufactured S1 and S2 samples, the average size of the equiaxed grains resulting from devitrification at the HAZ of the single track manufactured on the fully amorphous Finemet substrate (Fig. 15) is significantly smaller (d_{ave}=117 ± 22 nm). This can be explained by considering that the fully amorphous substrate was produced by induction casting, a process involving lower cooling rates than LPBF (typical cooling rates reach values of the order of 10^4 °C/s

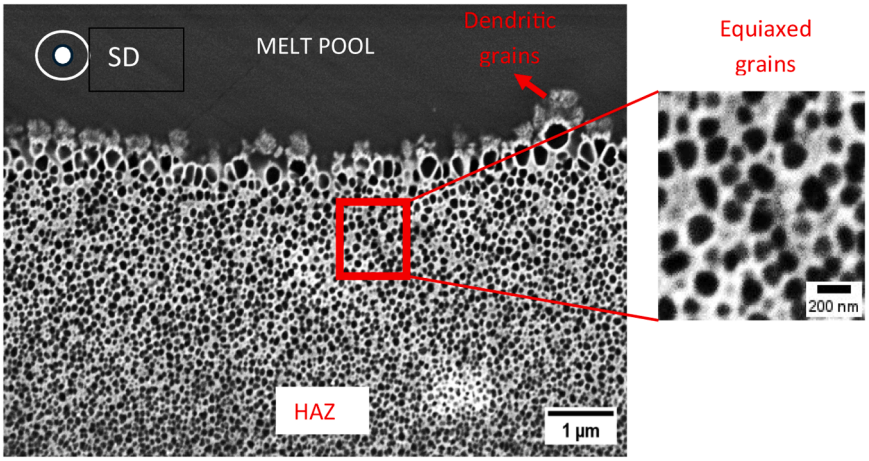

Fig. 15. Representative SEM micrograph illustrating at different magnifications the crystalline region surrounding the single-track melt pool that was melted over an amorphous Finemet substrate. Crystallites are preferentially etched, and they thus appear as dark regions.

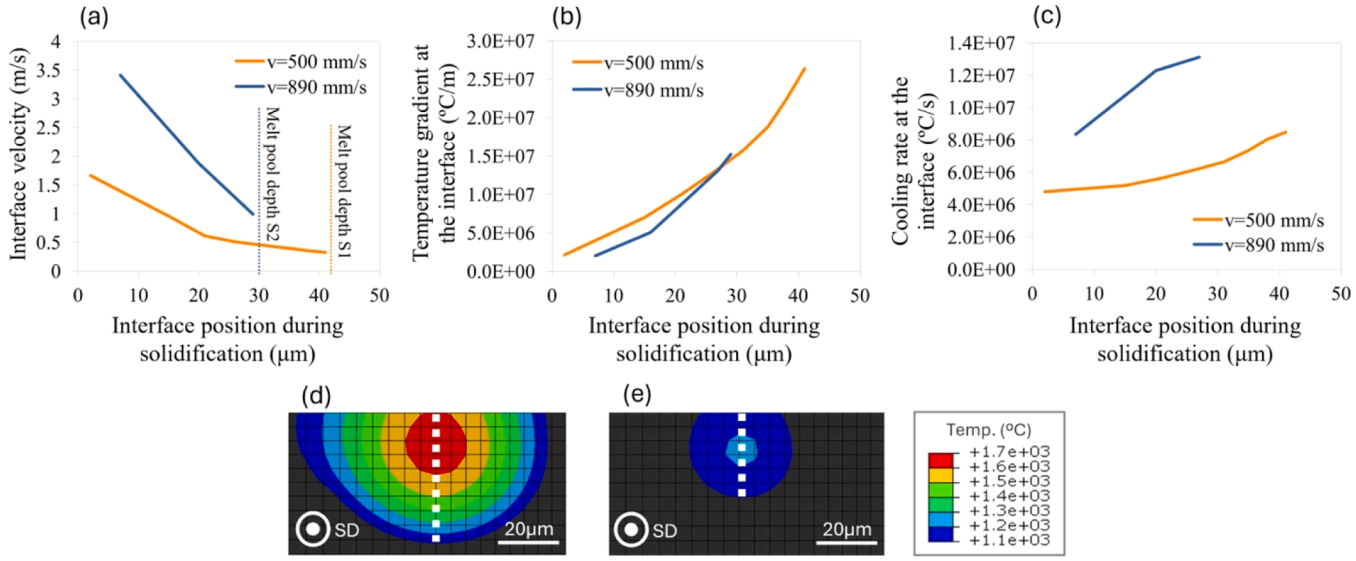

Fig. 16. Variation of (a) the interface velocity, (b) the temperature gradient at the interface, and (c) the cooling rate at the interface as a function of the solid/liquid interface position during solidification along the white dotted path indicated in (d) and (e) for S1 and S2 melt pools, respectively. The color scalebar in (d,e) represents the maximum temperature (in °C) reached during the solidification process. The interface position equal to 0 μm in (d) and (e) is located at the top of the melt pools.

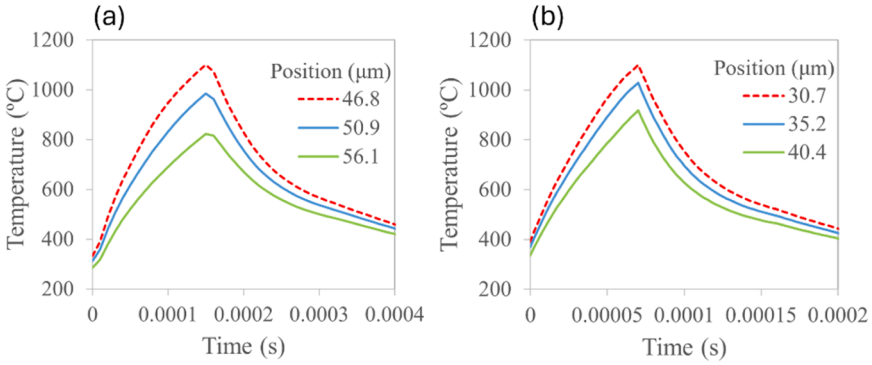

Fig. 17. FEM-simulated thermal profile corresponding to several locations within the HAZ in the vicinity of the melt pool boundary in samples (a) S1 and (b) S2. The numbers in the legend indicate the distance (position) at which the profiles were simulated with respect to the top of the corresponding melt pool.

[6]). Thus, a higher density of Cu clusters, and thus enhanced nucleation, is expected in the fully amorphous substrate produced by induction casting.

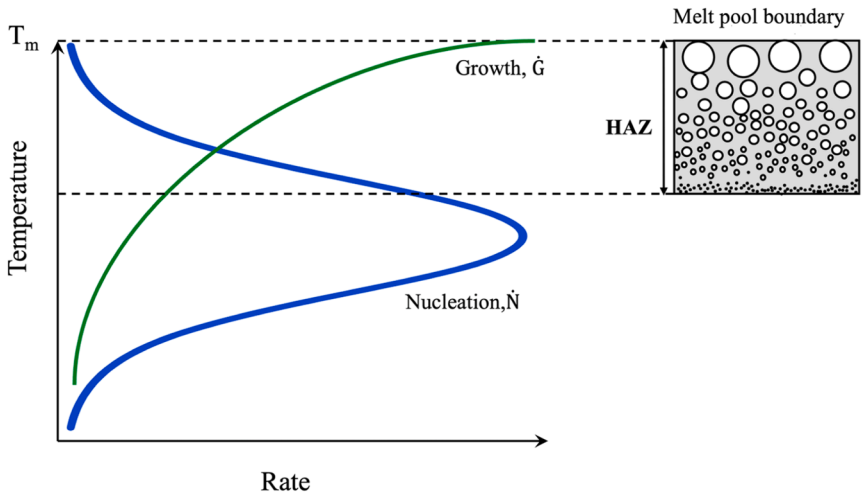

Fig. 18. Schematic diagram illustrating the origin of the gradient crystalline structure in the HAZ of the LPBF-manufactured samples as interpreted from the classical nucleation and growth theory.

4.3. Outline

This study suggests that the fabrication of nanocrystalline, complex-geometry FINEMET components with optimized soft-magnetic properties via LPBF could be pursued through two alternative routes. On the one hand, processing parameters could be adjusted to increase cooling rates, thereby suppressing Cu clustering and rendering the LPBF-deposited amorphous phase more resistant to devitrification during subsequent laser passes and layer deposition. Nanocrystallization would then be induced through tailored post-processing heat treatments. However, this approach is expected to generate elevated residual stresses, which may promote crack formation.

Alternatively, the processing parameters could be tuned to reduce cooling rates, thereby enhancing Cu clustering and increasing the density of in-situ nucleation sites. This could promote controlled nanocrystallization during LPBF, ideally leading directly to the formation of the desired nanostructure without the need for extensive post-processing.

5. Conclusions

This work aims to investigate crystallization during laser powder bed fusion of the soft magnetic metallic glass alloy Finemet. With that goal, two samples were manufactured using a double scanning strategy where the first pass is printed with common parameters, for powder densification, and the second pass is carried out using two different scan speeds (500 mm/s in sample S1 and 890 mm/s in sample S2). Densities between 92% and 94% are achieved under these conditions, as the manufactured samples inevitably contain unwanted cracks and pores. Crystallization in both samples is investigated using a combined approach including optical, scanning and transmission and electron microscopy, as well as finite element modeling of the solidification process and of the temperature evolution in the HAZ. The following conclusions are drawn from the current study:

1. Irrespective of the processing conditions, crystallization takes place mainly by devitrification of the previously deposited amorphous layer within the so-called heat affected zone. Devitrified crystals of equiaxed morphology are embedded in an amorphous matrix and they present a DO_3 structure. They are mainly formed by Fe and Si, while Nb and B partition to the amorphous matrix.
2. The crystals resulting from devitrification in the heat affected zone are significantly larger (d~ 40–50 nm to 400 μm) than the crystallites forming during isothermal annealing (d~10–20 nm). This is due, first, to the fact that the higher cooling rates in LPBF compared to melt spinning limit short range diffusion and lead to a smaller density of Cu clusters, and thus of crystallite nuclei. Second, enhanced grain growth is promoted due to the extreme temperatures inherent to the intrinsic heat treatment.
3. The wide size distribution of the grains that form by devitrification during LPBF in comparison with the nanocrystals forming during isothermal annealing of melt spun ribbons is mainly attributed to local variations in the thermal history within the heat affected zone, which lead to a wide spectrum of nucleation and growth rates.
4. A minor fraction of crystals, located at the bottom of melt pools, form during solidification in the two investigated samples. These crystals possess a dendritic morphology and a DO_3 structure, grow parallel to the build direction, and are mainly formed by Fe and Si. The size of these dendritic grains decreases with increasing scan speed, as high speeds are associated with higher cooling rates at the bottom of melt pools.
5. The FINEMET alloy was originally designed in a way that fully amorphous as-spun ribbons could judiciously be partially devitrified after the winding into a composite of Fe_3Si nanocrystallites embedded in an amorphous matrix to enhance the soft magnetic properties for passive motor components. However, here we have shown that during additive manufacturing via LPBF the crystallization takes place in-situ. It occurs partially during the solidification of the melt pool and also in the heat affected zone of the glassy layer underneath. This work concludes that, in order to manufacture a nanocrystalline-amorphous composite with a complex geometry using LPBF, which can be used as a passive motor component (e.g. a rotor or stator), the selection of parameters should aim at lowering the cooling rates and thereby increasing the nucleation rate to suppress the formation of large grains and to only trigger the formation of nanocrystals in the HAZ, as observed in Fig. 4. Additionally, elimination of defects such as cracks and pores remains to be addressed. Different strategies leading to an appropriate redistribution of the thermal energy, including for example heating of the substrate or advanced scanning strategies, must be combined with alloy design to achieve this goal.

CRediT authorship contribution statement

Perez-Prado Maria-Teresa: Writing – original draft, Visualization, Supervision, Resources, Project administration, Methodology, Funding acquisition, Formal analysis, Conceptualization. **Gallino Isabella:** Writing – review & editing, Supervision, Resources, Funding acquisition.

Ghavimi Amirhossein: Methodology, Investigation. **Busch Ralf:** Supervision, Resources, Funding acquisition. **Yang Biao Biao:** Methodology, Investigation. **Rodríguez-Sánchez Marcos:** Methodology, Investigation. **S. Sadanand:** Writing – review & editing, Writing – original draft, Visualization, Validation, Methodology, Investigation, Formal analysis. **Boccardo A. D.:** Writing – review & editing, Visualization, Software, Methodology, Investigation, Formal analysis.

Declaration of Competing Interest

The authors declare that they have no known competing financial interests or personal relationships that could have appeared to influence the work reported in this paper.

Acknowledgments

This work has been carried out under the scope AM2SoftMag project, funded by the European Innovation Council through the HORIZON-EIC-2021-PATHFINDEROPEN-01 grant (GA: 101046870). The authors thank the rest of the AM2SoftMag partners for their involvement in the project. Funding from the Spanish Ministry of Science and Innovation under projects PID2024–157137OB-C21 and PID2024–157137OA-C22 is also acknowledged. Teresa Nieto Valeiras is kindly thanked for her assistance with LPBF trials.

Appendix A. Supporting information

Supplementary data associated with this article can be found in the online version at doi:10.1016/j.addma.2026.105165.

Data availability

Data will be made available on request.

References

[1] A.L. Greer, M.B. Costa, O.S. Houghton, Metallic glasses, MRS Bull. 48 (2023) 1054–1061.
[2] W.L. Johnson, Bulk glass forming metallic alloys: science and technology, MRS Bull. 24 (1999) 42–56.
[3] A. Inoue, Stabilization of metallic supercooled liquid and bulk amorphous alloys, Acta Mater. 48 (2000) 279–306.
[4] R. Busch, J. Shroers, Thermodynamics and kinetics of bulk metallic glasses, MRS Bull. 32 (2007) 620–623.
[5] J. Löffler, Bulk metallic glasses, Intermetallics 11 (2003) 529–540.
[6] W.H. Wang, C. Dong, C.H. Shek, Bulk metallic glasses, Mater. Sci. Eng. R. 44 (2004) 45–89.
[7] J. Schroers, Bulk metallic glasses, Phys. Today 66 (2013) 32–37.
[8] W. Klement, R. Willens, P. Duwez, Non-crystalline structure in solidified gold–silicon alloys, Nature 187 (1960) 869–870.
[9] J. Kruzic, Bulk metallic glasses as structural materials: a review, Adv. Eng. Mater. 8 (2016) 1308–1331.
[10] M. Ashby, A.L. Greer, Met. Glass Struct. Mater. 54 (2006) 321–326.
[11] P. Tiberto, M. Baricco, E. Olivetti, R. Piccin, Magnetic properties of bulk metallic glasses, Adv. Eng. Mater. 9 (2007) 468–474.
[12] J.R. Scully, A. Gebert, J.H. Payer, Corrosion and related mechanical properties of bulk metallic glasses, J. Mater. Res. 22 (2007) 302–313.
[13] H.F. Li, Y.F. Zheng, Recent advances in bulk metallic glasses for biomedical applications, Acta Biomater. 36 (2016) 1–10.
[14] W.H. Wang, Bulk metallic glasses with functional physical properties, Adv. Mater. 21 (2009) 4524–4544.
[15] S. Sohrabi, J. Fu, L. Li, Y. Zhang, X. Li, F. Sun, J. Ma, W.H. Wang, Manufacturability of metallic glass components: processes, structures and properties, Prog. Mater. Sci. 144 (2024) 101286.
[16] I. Gallino, R. Busch, Physical Aging Studies in Bulk Metallic Glasses, in: Physical Metallurgy of Bulk Metallic Glass-Forming Liquids. Springer Series in Materials Science, 341, Springer, 2024.
[17] I. Gallino, R. Busch, Relaxation Pathways in Metallic Glasses, JOM 69 (2017) 2171–2177.
[18] R. Busch, I. Gallino, Kinetics, Thermodynamics, and Structure of Bulk Metallic Glass Forming Liquids, JOM 69 (2017) 2178–2186.
[19] A.L. Greer, Crystallization in metallic glasses, Mater. Sci. Eng. A 179/180 (1994) 41–45.
[20] T. Kulik, Nanocrystallization of metallic glasses, J. NonCryst. Solids 287 (2001) 145–161.
[21] L.M. Ruschel, B. Adam, O. Gross, N. Neuber, M. Frey, H.-J. Wachter, R. Busch, Development and optimization of novel sulfur-containing Ti-based bulk metallic glasses and the correlation between primarily crystallizing phases, thermal stability and mechanical properties, J. Alloy. Comp. 960 (2023) 170614.
[22] E. Pekarskaya, J.F. Löffler, W.L. Johnson, Microstructural studies of crystallization of a Zr-based bulk metallic glass, Acta Mater. 51 (2003) 4045–4057.
[23] Z. Yan, K. Song, Y. Hu, J. Eckert, Localized crystallization in shear bands of a metallic glass, Sci. Rep. 6 (2016) 19358.
[24] K. Zhang, Y. Wang, W. Zhang, Z. Hu, B. Wei, Y. Feng, Crystallization behavior and mechanical response of metallic glass induced by ion irradiation at elevated temperature, J. Nucl. Mater. 545 (2021) 152618.
[25] H.X. Li, Z.C. Lu, S.L. Wang, Y. Wu, Z.P. Lu, Fe-based bulk metallic glasses: Glass formation, fabrication, properties and applications, Prog. Mater. Sci. 103 (2019) 235–318.
[26] C. Suryanarayana, A. Inoue, Iron-based bulk metallic glasses, Int. Mater. Rev. 58 (2013) 131–166.
[27] G. Herzer, Modern soft magnets: Amorphous and nanocrystalline materials, Acta Mater. 61 (2013) 718–734.
[28] T. Gheiratmand, H.R. Madaah Hosseini, Finemet nanocrystalline soft magnetic alloy: Investigation of glass forming ability, crystallization mechanism, production techniques, magnetic softness and the effect of replacing the main constituents by other elements, J. Magn. Magn. Mater. 408 (2016) 177–192.
[29] M.E. McHenry, M.A. Willard, D.E. Laughlin, Amorphous and nanocrystalline materials for applications as soft magnets, Prog. Mater. Sc. 44 (1999) 291–433.
[30] K. Hono, D.H. Ping, M. Ohnuma, H. Onodera, Cu clustering and Si partitioning in the early crystallization stage of an Fe73.5Si13.5B9Nb3Cu1 amorphous alloy, Acta Mater. 47 (1999) 997–1006.
[31] H. Shivaee, A. Castellero, P. Rizzi, P.M. Tiberto, H. Hosseini, M. Baricco, Effects of chemical composition on nanocrystallization kinetics, microstructure and magnetic properties of finemet-type amorphous alloys, Met. Mater. Int. 19 (2013) 643–649.
[32] T. DebRoy, H.L. Wei, J.S. Zuback, T. Mukherjee, J.W. Elmer, J.O. Milewski, A. M. Beese, A. Wilson-Heid, A. De, W. Zhang, Additive manufacturing of metallic components – Process, structure and properties, Prog. Mater. Sci. 92 (2018) 112–224.
[33] N. Sohrabi, J. Jhabvala, R.E. Logé, Additive manufacturing of bulk metallic glasses—process, challenges and properties: a review, Metals 11 (2021) 1279.
[34] P. Zhang, J. Tan, Y. Tian, H. Yan, Z. Yu, Research progress on selective laser melting (SLM) of bulk metallic glasses (BMGs): a review, Int. J. Adv. Manuf. Technol. 118 (2021) 2017–2057.
[35] C. Zhang, D. Ouyang, S. Pauly, L. Liu, 3D printing of bulk metallic glasses, Mater. Sci. Eng. R. Rep. 145 (2021) 100625.
[36] H.R. Lashgari, M. Ferry, S. Li, Additive manufacturing of bulk metallic glasses: Fundamental principle, current/future developments and applications, J. Mater. Sci. Technol. 119 (2022) 131–149.
[37] N. Sohrabi, T. Ivas, J. Jhabvala, J.E.K. Schawe, J.F. Löffler, H. Ghasemi-Tabasi, R. E. Logé, Quantitative prediction of crystallization in laser powder bed fusion of a Zr-based bulk metallic glass with high oxygen content, Mater. Des. 239 (2024) 112744.
[38] Y. Lu, S. Su, S. Zhang, Y. Huang, Z. Qin, X. Lu, W. Chen, Controllable additive manufacturing of gradient bulk metallic glass composite with high strength and tensile ductility, Acta Mater. 206 (2021) 116632.
[39] X. Zhang, Y.H. Chueh, C. Wei, Z. Sun, J. Yan, L. Li, Additive manufacturing of three-dimensional metal-glass functionally gradient material components by laser powder bed fusion with in situ powder mixing, Addit. Manuf. 33 (2020) 101113.
[40] S. Hadibeik, E. Gingl, L. Schretter, B. Bochtler, J. Li, C. Gammer, A. Hohenwarter, J. Fl. Spieckermann, Eckert, Semi-analytical and experimental heat input study of additively manufactured Zr-based bulk metallic glass: Insights into nano- and global-scale relaxation and crystallization, Addit. Manuf. 89 (2024) 104295.
[41] B. Li, V. Yakubov, K. Nomoto, S.P. Ringer, B. Gludovatz, X. Li, J.J. Kruzic, Superior mechanical properties of a Zr-based bulk metallic glass via laser powder bed fusion process control, Acta Mater. 266 (2024) 119685.
[42] Z. Yang, M. Markl, C. Körner, Predictive simulation of bulk metallic glass crystallization during laser powder bed fusion, Addit. Manuf. 59 (2022) 103121.
[43] J.J. Marattukalam, V. Pacheco, D. Karlsson, L. Riekehr, J. Lindwall, F. Forsberg, U. Jansson, M. Sahlberg, B. Hjörvarsson, Development of process parameters for selective laser melting of a Zr-based bulk metallic glass, Addit. Manuf. 33 (2020) 101124.
[44] S. Hadibeik, H. Ghasemi-Tabasi, A. Burn, S. Lani, F. Spieckermann, J. Eckert, Controlling the glassy state toward structural and mechanical enhancement: additive manufacturing of bulk metallic glass using advanced laser beam shaping technology, Adv. Funct. Mater. 34 (2024) 2311118.
[45] X.P. Li, M.P. Roberts, S.O. Keeffe, T.B. Sercombe, Selective laser melting of Zr-based bulk metallic glasses: Processing, microstructure and mechanical properties, Mater. Des. 112 (2016) 217–226.
[46] S. Pauly, C. Schricker, S. Scudino, L. Deng, U. Kühn, Processing a glass-forming Zr-based alloy by selective laser melting, Mater. Des. 135 (2017) 133–141.
[47] J. Wagner, M. Frey, M. Piechotta, N. Neuber, B. Adam, S. Platt, L. Ruschel, S. S. Riegler, H.R. Jiang, G. Witt, R. Busch, S. Kleszczynski, Influence of powder characteristics on the structural and mechanical properties of additively manufactured Zr-based bulk metallic glass, Mater. Des. 209 (2021) 109976.
[48] L. Deng, S. Wang, P. Wang, U. Kühn, S. Pauly, Selective laser melting of a Ti-based bulk metallic glass, Mater. Lett. 212 (2018) 346–349.
[49] M. Frey, J. Wegner, E.S. Barreto, L. Ruschel, N. Neuber, B. Adam, S.S. Riegler, H. R. Jiang, G. Witt, N. Ellendt, V. Uhlenwinkel, S. Kleszczynski, R. Busch, Laser powder bed fusion of Cu-Ti-Zr-Ni bulk metallic glasses in the Vit101 alloy system, Addit. Manuf. 66 (2023) 103467.

[50] M. Frey, J. Wegner, L. Ruschel, E.S. Barreto, S.S. Riegler, B. Adam, N. Ellendt, S. Kleszczynski, R. Busch, Additive manufacturing of Ni62Nb38 metallic glass via laser powder bed fusion, Prog. Addit. Manuf. 10 (2025) 6797–6804.
[51] H.Y. Jung, S.J. Choi, K.G. Prashanth, M. Stoica, S. Scudino, S. Yi, U. Kühn, D. H. Kim, K.B. Kim, J. Eckert, Fabrication of Fe-based bulk metallic glass by selective laser melting: a parameter study, Mater. Des. 86 (2015) 703–708.
[52] S. Sadanand, M. Rodríguez-Sánchez, A. Ghavimi, R. Busch, P. Sharangi, P. Tiberto, E. Ferrara, G. Barrera, L. Thorsson, H.J. Wachter, I. Gallino, M.T. Pérez-Prado, Laser powder bed fusion of a Finemet-based alloy for soft magnetic applications, J. Laser Appl. 36 (2024) 042029.
[53] H. Wang, Selective laser melting of Finemet soft magnetic material. MSc thesis, Polytechnic Institute and State University, Virginia, 2023.
[54] M. Rodríguez-Sánchez, S. Sadanand, A. Ghavimi, R. Busch, P. Tiberto, E. Ferrara, G. Barrera, L. Thorsson, H.J. Wachter, I. Gallino, M.T. Pérez-Prado, Relating laser powder bed fusion process parameters to (micro)structure and to soft magnetic behaviour in a Fe-based bulk metallic glass, Materialia 35 (2024) 102111.
[55] L. Thorsson, M. Unosson, M.T. Pérez-Prado, X. Jin, P. Tiberto, G. Barrera, B. Adam, N. Neuber, A. Ghavimi, M. Frey, R. Busch, I. Gallino, Selective laser melting of a Fe-Si-Cr-B-C-based complex-shaped amorphous soft-magnetic electric motor rotor with record dimensions, Mater. Des. 215 (2022) 110483.
[56] G. Pozo López, L.M. Fabietti, A.M. Cond, S.E. Urreta, Microstructure and soft magnetic properties of Finemet-type ribbons obtained by twin-roller melt-spinning, J. Magn. Magn. Mater. 322 (2010) 3088–3093.
[57] T. Gheiratmand, H.R.M. Hosseini, P. Davami, F. Ostadhossein, M. Song, M. Gjoka, On the effect of cooling rate during melt spinning of FINEMET ribbons, Nanoscale 5 (2013) 7520–7527.
[58] H. Liu, Q. Jiang, J. Huo, Y. Zhang, W. Yang, X. Li, Crystallization in additive manufacturing of metallic glasses: a review, Addit. Manuf. 36 (2020) 101568.
[59] Y.G. Nam, B. Koo, M.S. Chang, S. Yang, J. Yu, Y.H. Park, J.W. Jeong, Selective laser melting vitrification of amorphous soft magnetic alloys with help of double-scanning-induced compositional homogeneity, Mater. Lett. 261 (2020) 127068.
[60] I. Arganda-Carreras, V. Kaynig, C. Rueden, K.W. Eliceiri, J. Schindelin, A. Cardona, H.S. Seung, Trainable Weka Segmentation: A machine learning tool for microscopy pixel classification, Bioinform 33 (2017) 2424–2426.
[61] D. Tourret, R. Tavakoli, A.D. Boccardo, A.K. Boukellal, M. Li, J. Molina-Aldareguia, Emergence of rapid solidification microstructure in additive manufacturing of a Magnesium alloy, Model. Simul. Mater. Sci. Eng. 32 (2024) 055012.
[62] M. Rodríguez-Sánchez, A.D. Boccardo, S. Sadanand, A. Ghavimi, R. Busch, P. Sharangi, E. Ferrara, G. Barrera, P. Tiberto, D. Tourret, I. Gallino, M.T. Pérez-Prado, Laser powder bed fusion of an Fe-based metallic glass using time delays, Addit. Manuf. 110 (2025) 104922.
[63] S. Price, B. Cheng, J. Lydon, K. Cooper, K. Chou, On process temperature in powder-bed electron beam additive manufacturing: model development and validation, J. Manuf. Sci. Eng. 136 (2014) 061019.
[64] E.A. Brandes, G.B. Brook. Smithells Metals Reference Book, seventh ed, Elsevier Inc, 2013.
[65] Alloy Phase Diagrams, ASM Handbook, 3, ASM International, 1992, p. 860.
[66] J.D. Ayers, V.G. Harris, J.A. Sprague, W.T. Elam, H.N. Jones, On the formation of nanocrystals in the soft magnetic alloy Fe73.5Nb3Cu1Si13.5B9, Acta Metall. Mater. 46 (1998) 1861–1874.
[67] D. Ouyang, N. Li, W. Xing, J. Zhang, L. Liu, 3D printing of crack-free high strength Zr-based bulk metallic glass composite by selective laser melting, Intermetallics 90 (2017) 128–134.
[68] Ł. Żrodowski, R. Wróblewski, M. Leonowicz, B.M. Morończyk, T. Choma, J. Ciftci, W. Wojciech Święszkowski, A. Dobkowska, E. Ura-Bińczyk, P. Błyskun, P. Błyskun, J. Jaroszewicz, A. Krawczyńska, K. Kulikowski, B. Wysocki, T. Cetner, G. Moneta, X. Li, L. Yuan, A. Małachowska, P.J. Masset, R. Chulist, C. Żrodowski, How to control the crystallization of metallic glasses during laser powder bed fusion? Towards part-specific 3D printing of in situ composites, Addit. Manuf. 76 (2023) 103775.
[69] S.V. Madge, A.L. Greer, Laser additive manufacturing of metallic glasses:issues in vitrification and mechanical properties, Oxf. Open Sci. 1 (1) (2021) itab015.
[70] G. Yang, X. Lin, F. Liu, Q. Hu, L. Ma, J. Li, W. Huang, Laser solid forming Zr-based bulk metallic glass, Intermetallics 22 (2012) 110–115.
[71] X.P. Li, C.W. Kang, H. Huang, L.C. Zhang, T.B. Sercombe, Selective laser melting of an Al86Ni6Y4.5Co2La1.5 metallic glass: Processing, microstructure evolution and mechanical properties, Mater. Sci. Eng. A 606 (2014) 370–379.
[72] K. Hono, K. Hiraga, Q. Wang, A. Inoue, T. Sakurai, The microstructure evolution of a Fe73.5 Sil3.5B9Nb3Cu1 nanocrystalline soft magnetic material, Acta Metall. Mater. 40 (1992) 2137–2147.
[73] N. Lecaude, J.C. Perron, Nanocrystallization mechanisms in Finemet-type alloys from calorimetric studies, Mater. Sci. Eng. 226-228 (1997) 581–585.
[74] D.R. Uhlmann, A kinetic treatment of glass formation, J. NonCryst. Solids 7 (1972) 337–348.
[75] V.I. Tkatch, A.I. Limanovskii, S.N. Denisenko, S.G. Rassolov, The effect of the melt-spinning processing parameters on the rate of cooling, Mater. Sci. Eng. A 323 (2002) 91–96.
[76] M. Matsuura, N. Nishijima, K. Takenaka, A. Takeuchi, H. Ofuchi, A. Makino, Evolution of fcc Cu clusters and their structure changes in the soft magnetic Fe85.2Si1B9P4Cu0.8 (NANOMET) and FINEMET alloys observed by X-ray absorption fine structure, J. Appl. Phys. 117 (2015) 17A324.
[77] B. Lohwongwatana, J. Schroers, W.L. Johnson, Strain rate induced crystallization in bulk metallic glass-forming liquid, Phys. Rev. Lett. 96 (2006) 075503.
[78] I. Gallino, P. Wadhwa, R. Busch, J. Phys. Condens. Matter 33 (2021) 474002.
[79] W.D. Callister, D.G. Rethwisch. Materials Science and Engineering, an introduction, 10th Edition, Wiley, 2018, p. 313.